


Structural evolution of vacancy clusters in α -iron: A kinetic activation-relaxation technique studyMd Mijanur Rahman^{1,*}, Fedwa El-Mellouhi,² and Normand Mousseau^{1,†}¹*Département de physique and Regroupement québécois sur les matériaux de pointe, Université de Montréal, C.P. 6128, Succursale Centre-Ville, Montréal, Québec, Canada H3C 3J7*²*Qatar Environment and Energy Research Institute, Hamad Bin Khalifa University, PoBox 34110, Doha, Qatar* (Received 19 December 2022; revised 20 July 2023; accepted 22 August 2023; published 11 September 2023)

The kinetics of vacancies in materials plays a significant role in determining their physical properties. In this work, we investigate diffusion of vacancies in α -iron using the kinetic activation-relaxation technique, an off-lattice kinetic Monte Carlo method with on-the-fly catalog building based on the activation-relaxation technique nouveau coupled with an embedded atom method potential. We focus on the evolution of one to eight vacancies to provide a detailed picture of the energy landscape, overall kinetics, and diffusion mechanisms associated with these defects. We show formation energies, activation barriers for the ground state of all eight systems, and migration barriers for the diffuse systems. This study points to an unsuspected dynamic richness, even for this simple system, that can only be discovered through comprehensive and systematic approaches such as the kinetic activation-relaxation technique. The complex energetic environment controlling the kinetics of small vacancy clusters, we find here, demonstrates that simple rules are not sufficient to develop a robust approach to predictive control and prevention of damage processes associated with vacancy clusters in structural metals.

DOI: [10.1103/PhysRevMaterials.7.093602](https://doi.org/10.1103/PhysRevMaterials.7.093602)

I. INTRODUCTION

Vacancies, isolated and in clusters, are key defect structures for determining a material's physical and mechanical properties. Vacancies are created inside materials under deformation [1,2], irradiation [3–5], or after quenching [6,7]. Once formed, they can further aggregate and form nanoscale defects, such as stacking faults, cracks, voids, gas bubbles, dislocation loops, etc. [8–11]. The subsequent evolution of these defect structures strongly affects the material's properties, producing effects such as embrittlement, strengthening, crack resistance, ductility, or creep behaviors [12–15], which can lead to property degradation and possibly component failure. Thus, understanding the formation and evolution of vacancy clusters is an interesting topic for materials used in extreme environments.

Despite decades of extensive research, understanding the formation and evolution of vacancy clusters remains a formidable challenge. The atomic-scale details of vacancy cluster diffusion are generally difficult to observe experimentally. Thus, atomistic simulations are needed to understand the interaction and migration of vacancy clusters at this scale. For this, however, we need a proper description, using either *ab initio* approaches or accurate empirical potentials, as well as comprehensive sampling methods. *Ab initio* calculations based on density functional theory (DFT) [16] provide an accurate approach to investigating atomic details and therefore have been used in numerous studies on vacancy clusters [17–23]. However, due to their costs, these methods offer

a limited capacity to sample energy landscape and most work limit themselves to finding a transition state between given initial and final states based on an initial guess for the connecting trajectory. Only the pathway closest to the initial guess is explored, leaving other possible pathways unexplored. This can be problematic with complex energy landscapes, where multiple nontrivial but relevant pathways may be present. Moreover, DFT methods are too expensive to apply to large systems or to allow extensive sampling. While standard simulation tools such as molecular dynamics [24] coupled with empirical potentials could provide useful information on atomistic details of these diffusion mechanisms, they often cannot reach the extended timescale over which many of these processes occur. Kinetic Monte Carlo approaches [25,26] provide a solution to reaching longtime dynamics; however, the standard implementation requires an upfront knowledge of the relevant barriers and cannot consider crucial elastic deformations. While results from such simulations are enlightening, their quantitative validity is limited since the full details of local atomic configurations can significantly affect diffusion kinetics. This is why we need a method such as the kinetic activation-relaxation technique (k-ART) [27,28], a unique off-lattice kinetic Monte Carlo algorithm with on-the-fly catalog-building capabilities, which lifts those limitations and allows us to map these processes in detail. The k-ART ensures an efficient and extensive sampling of energy landscapes as it incorporates exact elastic effects at both minima and saddle points for a precise kinetic description of complex materials ranging from defects in metals to the long-time evolution of amorphous materials [29–32].

In this study, we focus on vacancy cluster diffusion in α -Fe, a central component of the ferritic steels widely used in aeronautic and nuclear industries. This system has

*md.mijanur.rahman@umontreal.ca

†normand.mousseau@umontreal.ca

received considerable attention over the years [18,19,33–46], with main efforts going towards elucidating the structure of the vacancy clusters formed during deformation or irradiation. It is well known, for example, that the most common vacancy clusters in α -Fe are cavities [34,35]. However, their formation mechanism and kinetic evolution are less well understood. An extensive characterization of vacancy cluster formation and possible diffusion pathways is still missing. Such a work would provide a complete picture of the various diffusion mechanisms and evaluate the possible richness of the energy landscape associated with this phenomenon.

For this purpose, we employ k-ART, coupled with a reliable and well-tested embedded atom method (EAM) potential, to achieve this goal. Using this approach, we characterize the associated energy landscape and clustering mechanisms of vacancy clusters. We focus, more specifically, on the diffusion and clustering of one to eight vacancies in crystalline α -iron. We show that even these simple assemblies, from one to eight vacancies, can present complex reorganizations that considerably affect their diffusion properties. The paper is organized as follows: The methodology, including a brief overview of k-ART, the model employed, and the computational details, are presented in Sec. II. Then, simulation results are presented and discussed in Secs. III and IV, respectively. Finally, the conclusion is given in Sec. V.

II. METHODOLOGY

A. Kinetic-activation relaxation technique (k-ART)

The k-ART is a kinetic Monte Carlo (KMC) algorithm with on-the-fly event catalog-building capacity and exact elasticity treatment. While details of k-ART implementation can be found elsewhere [27,28,47], here we provide a brief overview of the basic algorithm and the specific parameters used in this study.

At the beginning of each KMC step, the local environment surrounding each atom is characterized by its local topology. The k-ART generates a local connectivity graph involving each atom and its surroundings. Here, we use a cutoff of 2.7 Å for drawing a link between two atoms and a radius of 6.0 Å around the central atom for the maximum graph size. Graphs are then analyzed using the NAUTY [48] package, a topological analysis package that it used to provide a unique identifier associated with the graph's automorphic group and the permutations allowing to restore of the reference graph. If the topology is known, events related to it are recovered from the catalog and placed in a KMC tree; otherwise, the catalog is updated by launching a series of activation-relaxation technique nouveau (ART nouveau or ARTn) [49–51] searches to identify the diffusion mechanisms associated with this topology. Once the catalog is fully updated and the tree is completed for the current atomistic configuration, generic events are ordered according to their rate, defined as

$$\Gamma_i = \nu_0 e^{-\frac{E_b}{k_B T}}, \quad (1)$$

where ν_0 is a fixed prefactor which is fixed at 10^{13} Hz and E_b , the activation energy for the event i defined as the energy difference between the transition state and the initial minimum [52–54]. Once the event tree is completed, the lowest-energy

barrier events that make up to 99.99% of the rate are fully reconstructed and reconverged into specific events. In this manner, low barriers are fully relaxed according to actual geometry and, therefore, exactly include short- and long-range elastic effects. Then the specific rates and overall KMC time step are estimated again with the refine barriers. Finally, the event is selected according to the standard KMC algorithm [26]. The elapsed time t is computed according to a Poisson distribution as

$$t = -\frac{\ln \mu}{\sum_i \Gamma_i}, \quad (2)$$

where μ is a random number uniformly distributed between 0 and 1. To avoid being trapped by low barrier events associated with nondiffusive mechanisms, we use the basin accelerated mean-rate method (bacMRM) [47,55], which solves them analytically. To fully characterize the kinetics on all relevant timescales, we start all simulations with a basin threshold of 0.1 eV and increase it as flickering occurs.

B. Force fields

Interactions are calculated using the large-scale atomic/molecular massively parallel simulator (LAMMPS) [56,57] by linking its library to k-ART. To speed up the computation, we use parallelization to generate events on multiple processors. In this study, we use the EAM potential developed by Ackland and Mendeleev [58] for Fe-Fe interactions. This potential provides an excellent agreement with DFT calculations in bulk Fe.

C. Simulation details

We characterize the diffusion pathways of vacancy clusters in a perfect cubic bcc bulk crystal containing 2000 Fe atoms with periodic boundary conditions. The supercell is oriented in the cubic directions, i.e., x in [100], y in [010], and z in [001]. For each system containing one to five and eight vacancies, we perform runs at 600 K, as defined in the calculation of the rate. The variation in the total energy of the system containing the largest cluster as a function of the box size was checked to ensure the size was sufficiently large. In all cases, the simulation box is a cubic box with a length of 28.553 Å, corresponding to a lattice parameter of 2.8553 Å in agreement with the literature for the bcc Fe structure. The system's energy is first minimized at $T = 0$ K using LAMMPS before k-ART simulations are launched.

The ground-state (GS) energy is defined for each simulation as the lowest-energy minimum identified during the run, E_{GS} . The activation energy for an event is defined as the energy difference between the initial minimum E_{min} and the adjacent saddle E_{sad} (i.e., the barrier crossed between two adjacent minima) or

$$E_b = E_{sad} - E_{min}. \quad (3)$$

The migration energy is defined as the difference between the energy of the highest saddle point crossed along a path connecting one local minimum to another and E_{min} .

The square displacement (SD) is computed as usual:

$$SD = \sum_i^N [r_i(t_n) - r_i(0)]^2, \quad (4)$$

where N is the number of vacancies and $r_i(t_n)$, the position of vacancy i at KMC step n .

To describe the energy cost for the formation of a vacancy cluster with respect to the perfect lattice, the formation energy per vacancy for the n -vacancy cluster is defined as

$$E_{nv}^f = \frac{E_{nv}^F}{n} = \frac{1}{n} \left(E_{N-n}^{\text{tot}} - \frac{N-n}{N} E_N^{\text{tot}} \right), \quad (5)$$

where E_{nv}^F is the formation energy for an n -vacancy cluster, E_{N-n}^{tot} is the total energy of the supercell with $(N-n)$ atoms and an n -vacancy cluster, and $E_N^{\text{tot}} = -8025.965$ eV is the total energy of the corresponding defect-free supercell containing N atoms (2000 atoms in our case).

To compare the thermodynamic stability of a vacancy cluster, the binding energy per vacancy for the n -vacancy cluster is given by

$$E_{nv}^b = \frac{1}{n} \left(\sum_n E_{1v}^f - E_{nv}^F \right) = E_{1v}^f - E_{nv}^f, \quad (6)$$

where $E_{1v}^f = 1.722$ eV is the formation energy of an isolated vacancy. Positive binding energy indicates a preference for the n -isolated vacancies to form an n -vacancy cluster, and higher binding energy denotes greater stability.

D. Elastic dipole tensors and relaxation volumes

The elements of the dipole tensor associated with a defect can be calculated according to the equation [59,60]

$$P_{ij} = -V_{\text{cell}} \sigma_{ij}, \quad (7)$$

where V_{cell} is the volume of the simulation cell and σ_{ij} is the difference between the average macroscopic stress in the cell containing the defect and in the pristine structure.

From the P_{ij} tensor associated with one of the local minima or saddle points, the relaxation volume of bound vacancy clusters in bcc iron can be easily determined in the context of the elastic model by the following equation:

$$V_{[\text{min}|\text{saddle}]}^{\text{rel}} = \frac{\text{Tr}(P_{ij})}{C_{11} + 2C_{12}}. \quad (8)$$

In this study, the elastic constants of the bcc iron matrix corresponding to the Fe-Fe potential, $C_{11} = 243$, $C_{12} = 145$, and $C_{44} = 116$ GPa, are in good agreement with the values of the experimental and DFT results [61,62]. The migration volume is defined as the difference between the relaxation volume of the highest saddle point crossed along a path connecting one local minimum to another and the initial minimum.

E. Vacancy structure notation

The complex vacancy configurations are described in terms of the vacancy-pair separation distances. The number of vacancy pairs in a m -vacancy structure is $P(m) = m!/[2!(m-2)!]$. For example, the bound structure of the trivacancy

complex has $P(3) = 3!/(2! \times 1!) = 3$ vacancy pairs. Using d_i to represent the separation distance between two vacancies that are i th neighbors, the bound structure of the m -vacancy complex can be described by these distances: $mV(N_{d_1}, N_{d_2}, N_{d_3}, N_{d_4}, N_{d_5}, N_{d_6})$, where N_{d_i} is the total number of i th nearest-neighbor (NN) distances between pairs of vacancies in the structure. For instance, $3V(2, 1, 0, 0, 0, 0)$ illustrates the bound cluster configuration with two 1NN and one 2NN vacancy-pair separation distances.

As discussed below, the binding energy for divacancies in the fifth and sixth neighboring configurations is below room temperature (at -0.021 and -0.011 eV, respectively). The inclusion of positions in the fifth and sixth neighbors is therefore sufficient to describe the aggregation kinetics.

F. Calculation of lifetimes

To study the vacancy cluster lifetime and diffusivity, we construct a complete transition matrix that allows recovering the associated rate of all the possible states where the system can move from the ground state until the system reaches a state where one of the vacancies in it moved further away than the fourth-nearest-neighbour (4NN) distance from any of the remaining cluster vacancies.

The diffusion coefficient and thermal lifetime are calculated using the Markov chain solution described as follows:

- (1) choose the ground state for a vacancy cluster of that size as initial state i ;
- (2) generate a uniform random number $u \in (0,1)$;
- (3) select the next event j probabilistically such that $\sum_k^{j-1} p_{ik} < u \leq \sum_k^j p_{ik}$, where p_{ik} is the probability to jump from state i to state k ;
- (4) update the current state $j \rightarrow i$;
- (5) generate a second uniform random number $\mu \in (0,1)$;
- (6) update times as $\tau = \tau - \frac{\ln \mu}{\sum_k \Gamma_k}$, where Γ_k is the transition rate from state i to state k ;
- (7) return to step 2.

The lifetime of the cluster is defined as the time at which one of the vacancies in it moves further away than the 4NN distance from any of the remaining cluster vacancies. Cluster mobility is studied by tracing the diffusion of the cluster. The same simulation is repeated $N_{\text{sim}} = 5$ million times in order to obtain sufficient statistics. The diffusion coefficient is calculated as

$$D = \frac{1}{N_{\text{sim}}} \sum_i^{N_{\text{sim}}} \frac{R_i^2}{6\tau_i}, \quad (9)$$

where R_i^2 is the squared displacement during the lifetime τ_i of the cluster, in simulation i .

III. RESULT

A. Validation

As a validation test, we analyze the diffusion of a single Fe vacancy. The formation energy of monovacancy calculated using EAM potential is 1.722 eV, consistent with previous simulations and experimental results (see Table. I). The vacancy self-diffusion takes place through a first-nearest-neighbor (1NN) jump with 100% probability. This 1NN jump

TABLE I. Formation energy (E_{nv}^F) of the ground state (GS) and migration energy (E^m) of the dominant diffusion mechanisms from one to eight vacancies. A comparison between the values obtained in this work (T.W.) and other works (O.W.), which are either experimental or, more often, *ab initio*, is also presented.

Cluster	E_{nv}^F (eV)		E^m (eV)	
	T.W.	O.W.	T.W.	O.W.
1V	1.722	1.81 [63], 1.95 [64]	0.640	0.640 [19], 0.670 [64]
$2V_{2NN-4NN}$	3.204	3.214 [65], 3.610 [64]	0.641	0.680 [17]
$2V_{2NN-1NN}$			0.716	0.76 [17]
3V	4.625		0.653	0.66 [46], 0.64 [18], 0.36 [19]
4V	5.763		0.703	0.72 [33]
5V	6.873		0.638	
8V	9.640		1.093	

occurs either through a direct transition, from the ground state GS (at $E_{GS} = -8020.231$ eV with relaxation volume -2.530 Å³) to a new GS by crossing an energy barrier of 0.64 eV (migration volume -1.625 Å³), or in two steps, from the GS to a metastable state at $E_{min} = 0.549$ eV above the GS (relaxation volume of the metastable state -3.189 Å³) by crossing an energy barrier of 0.64 eV (activation volume -1.625 Å³); from this state, a second barrier with a 0.091 eV (activation volume -0.956 Å³) energy brings the system back into a new GS. The barrier heights and migration volumes are in good agreement with the results of both experiments and DFT simulations [18,42,61].

For further validation, the interactions between two vacancies are analyzed, as they are positioned in the first-, second-, third-, fourth-, fifth-, and sixth-nearest-neighbor sites of each other (denoted as 1NN, 2NN, 3NN, 4NN, 5NN, and 6NN sites). The interaction for the 2NN state is strongly attractive (with a binding energy of approximately 0.240 eV), as seen in previous studies [17,18,41], while it is only slightly attractive for the 1NN and 4NN states (with a binding energy of 0.141 and 0.029 eV, respectively). For their part, 3NN, 5NN, and 6NN sites show a negative binding energy of -0.022 , -0.021 , and -0.011 eV, respectively, indicating a repulsive interaction. For larger clusters, the most stable configurations tend to maximize the number of 2NN and 1NN vacancy pair-separation distances.

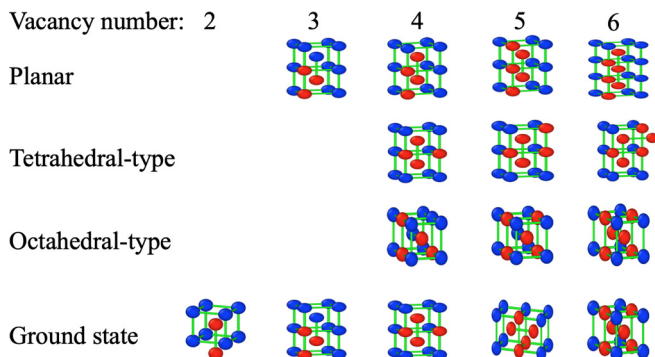


FIG. 1. Schematic representation of the configurations for planar and body clusters with one to six vacancies. Blue and red circles represent crystalline Fe atoms and vacancies, respectively.

B. Structure and stability

To proceed further, we analyze the thermal stability of the clusters, which are classified into three groups according to the shape characteristics of the initial clusters: Linear, planar, and body clusters. Vacancies in the linear clusters are positioned along either [100], [110], or [111] directions, respectively. The planar clusters lie on the [110] plane. The body clusters are separated into two groups: Tetrahedral type, with tetrahedral features or *s* combination of the tetrahedron; and octahedral type, which tends to form octahedral structure based on the relevance of cluster structures. The configurations for the planar and body clusters with two–six vacancies are shown in Fig. 1.

Figure 2 presents the formation and binding energies per vacancy for different cluster types as functions of vacancy number. The binding energy generally increases with the vacancy number for each cluster type, indicating the preference for further cluster growth. Moreover, the binding energies for

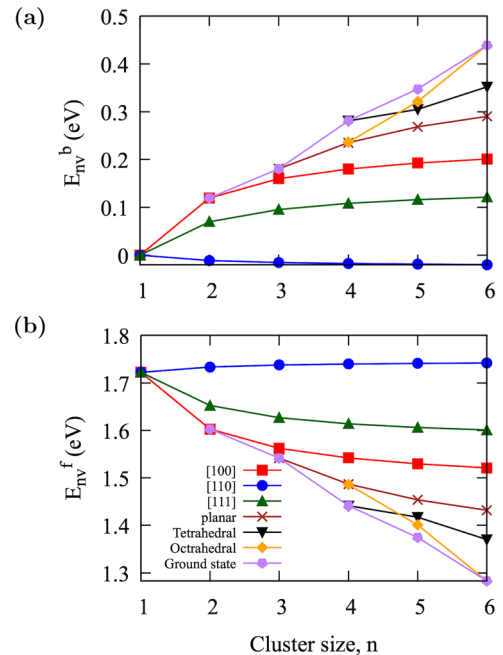


FIG. 2. (a) Binding energies and (b) formation energies for different vacancy cluster types in α -iron.

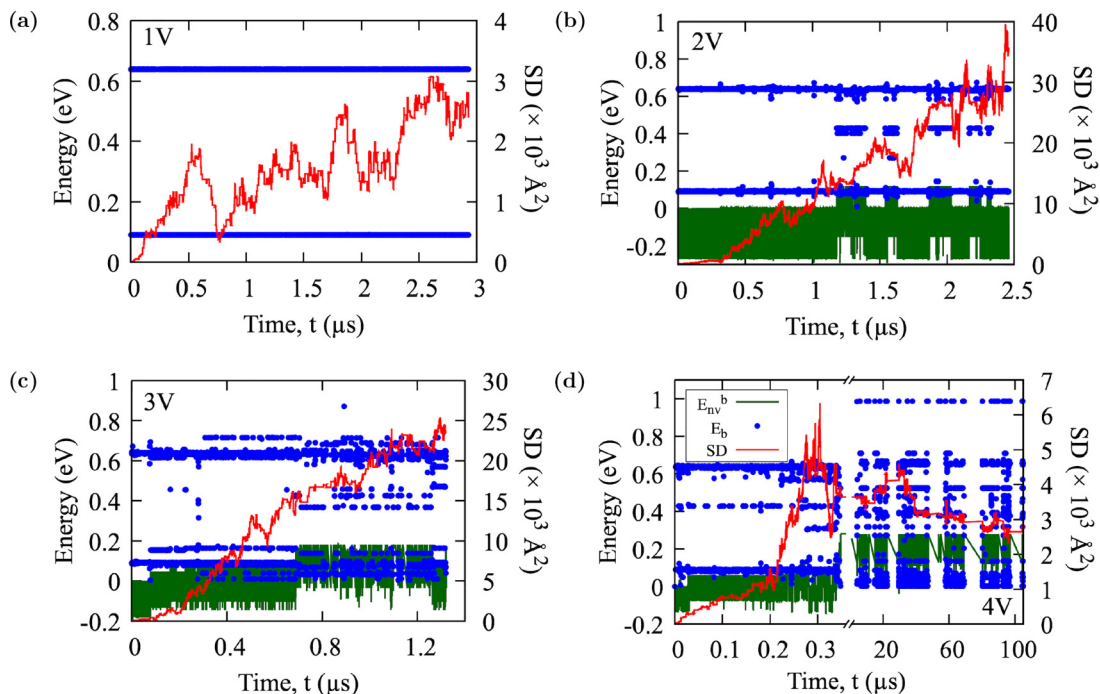


FIG. 3. Activation-energy (left, blue symbols), binding energy at the local minima (left, green line), and squared displacement (right, red line) as a function of time for one to four Fe vacancies in a bcc crystal at 600 K: (a) one, (b) two, (c) three, and (d) four vacancies.

the tetrahedral- and octahedral-type clusters are higher and have larger energy gradients. In contrast, the binding energies of the linear and planar clusters are lower and have smaller gradients. This is expected as the tetrahedral- and octahedral-type clusters, with lower surface to volume ratio, should be more stable and have higher growth tendencies.

C. Small vacancy clusters (two–four vacancies)

We now turn to vacancy aggregation and diffusion mechanisms of small vacancy clusters containing two to four vacancies. Simulations start with the defects placed at a large enough distance (around 10.2 \AA) from each other to ensure minimal interaction. The detailed activation energy, binding energy at the local minima, and squared displacement as a function of time for two to four Fe vacancies in a bcc crystal at 600 K are shown in Fig. 3. The selected activation energies as a function of the KMC step, as well as the number of events in the catalog per step for events involving vacancy movement, are shown in Fig. S1 in the Supplemental Material [66]. The schematic representation and energetic descriptions of the dominant diffusion mechanisms are shown in Fig. 4.

Due to elastic interactions, the two vacancies aggregate rapidly, in less than $1.2 \mu\text{s}$ (2173 KMC steps), into a dimer with the two-point defects at a 2NN distance from each other; this represents a ground state with a formation energy 3.204 eV (relaxation volume -5.684 \AA^3). Table II summarizes the energy landscape for the divacancy complex and provides information regarding the formation, binding, and migration energies. Table III indicates the relaxation volume and migration volume for states with vacancies in the first- to sixth-nearest-neighbor positions. The divacancy migrates

through two dominant pathways, where the configuration changes from the second nearest neighbor (GS) to the first-nearest neighbor and back to the second-nearest neighbor and from the second-nearest neighbor to the fourth-nearest neighbor and back to the second-nearest neighbor. The energy barrier for each of these migration paths is indicated in Fig. 5, where the green line represents the energy barrier for migration via the first-nearest-neighbor configuration, and the blue line represents the energy barrier for migration via the fourth-nearest-neighbor configuration. Mostly, the divacancy migrates by oscillating between the 2NN and 4NN states, with an energy barrier of 0.641 eV (migration volume -1.637 \AA^3). The 1NN pathway may be expected to be the dominant mechanism, as one may predict the transition to the lower-energy 1NN state to have a lower-energy barrier. However, the 2NN to 1NN transition has an energy barrier of 0.716 eV (migration volume -0.964 \AA^3), making it kinetically less favorable. The diffusion mechanisms and barrier heights match previous studies using either *ab initio* approaches or empirical potentials (see Table I) [17].

The three isolated vacancies aggregate to form the ground state in $0.71 \mu\text{s}$ and 1583 KMC steps, with two 1NN and one 2NN vacancy pair-separation distances, forming an isosceles triangle. This cluster is characterized by a binding energy of 0.68 eV (0.23 eV per vacancy) as measured from the three isolated vacancies having a relaxation volume -6.264 \AA^3 . Once vacancies reach the ground state, eight configurations dominate the dynamics of the system, representing more than 95% of all accepted configurations. Table IV summarizes the energy landscape for the eight most stable trivacancies bound compounds, providing information regarding formation, and migration energies for states and Table V represents the relaxation volume and migration volume for these states. The

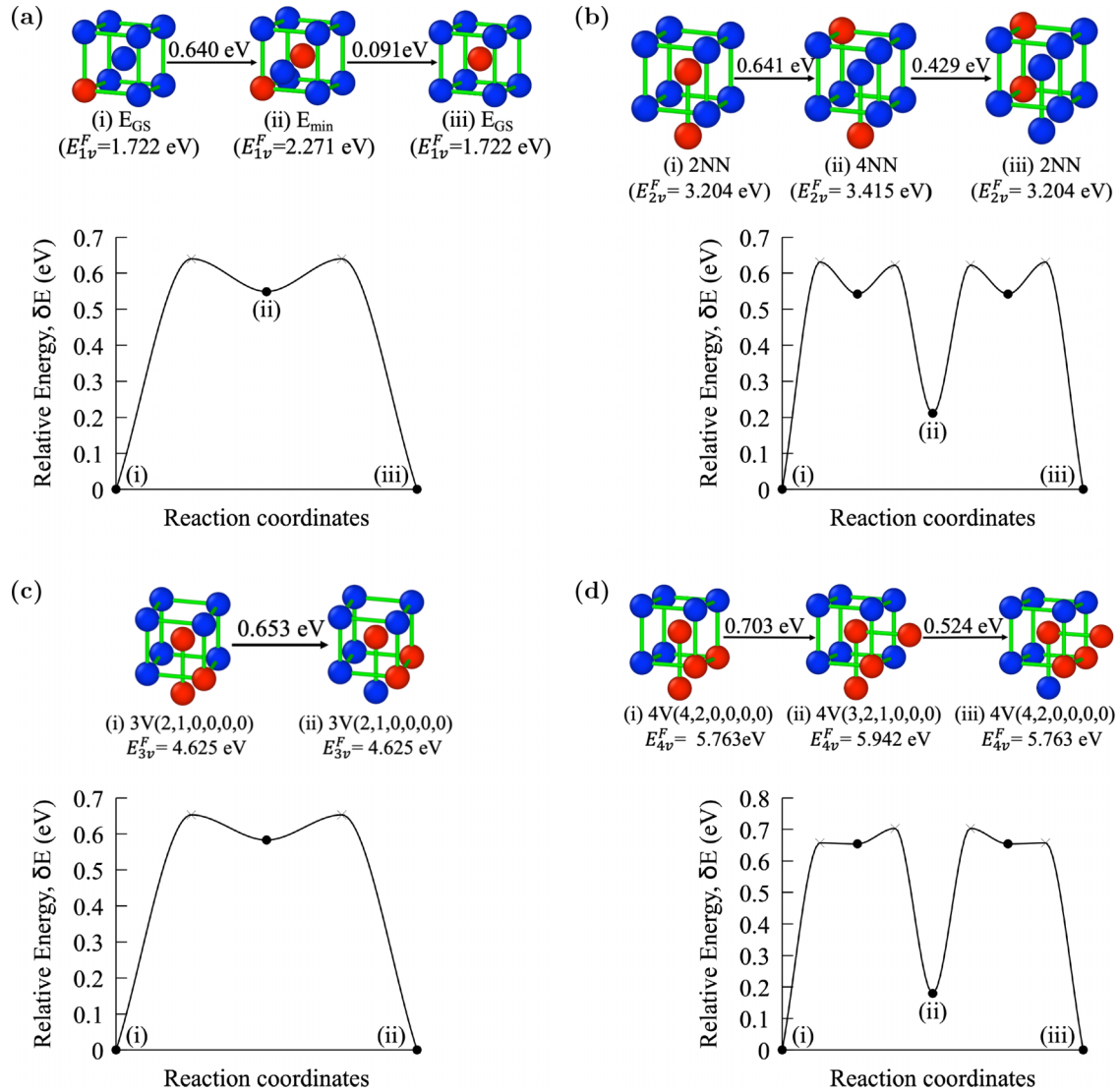


FIG. 4. Schematic representation and energetic descriptions of the dominant diffusion path for (a) one, (b) two, (c) three, and (d) four vacancies in bcc Fe at 600 K. In the schematic diagrams, the blue and red spheres represent crystalline Fe atoms and vacancies, respectively. In the energetic description, the cross and filled circle represent the saddle points and minima, respectively. The indices (I, II, and III) are used to identify states and explain the diffusion mechanism. The bound structures of three and four vacancies are indicated as $3V(N_{d_1}, N_{d_2}, N_{d_3}, N_{d_4}, N_{d_5}, N_{d_6})$ and $4V(N_{d_1}, N_{d_2}, N_{d_3}, N_{d_4}, N_{d_5}, N_{d_6})$, respectively. Where $N_{d_1}, N_{d_2}, N_{d_3}, N_{d_4}, N_{d_5}$, and N_{d_6} represent the total number of 1NN, 2NN, 3NN, 4NN, 5NN, and 6NN vacancy-pair-separation distances, respectively.

TABLE II. Formation energies (E_{nv}^F), binding energies (E_{nv}^b), and migration energies (in eV) for pathways between the six dominant bound states for the divacancy complex.

To \ From						
	1NN	2NN	3NN	4NN	5NN	6NN
E_{nv}^F	3.303	3.204	3.466	3.415	3.465	3.455
E_{nv}^b	0.141	0.240	-0.022	0.029	-0.021	-0.011
1NN		0.716	0.694		0.577	
2NN	0.617			0.429		
3NN	0.857			0.676		
4NN		0.641	0.626		0.589	0.630
5NN	0.738			0.638		
6NN				0.670		

dominant diffusion mechanism for the trivacancy bound compound is a one-step process associated with a rotation that involves migrating one vacancy from the ground state to a first-neighbor site without breaking the triangle, crossing a barrier of 0.653 eV (migration volume -1.920 \AA^3) shown in Fig. 4. The barrier height is in good agreement with previous literature results (see Table 1) [18,46]. The cluster is stable and can be broken only by crossing a 0.691-eV barrier, which involves migrating a vacancy to a nearest-neighbor site forming a complex of two 2NN and one 3NN vacancy pair-separation distance, 0.084 eV above the GS. Then from this state, the system is back into a new GS by crossing a second barrier with an energy of 0.605 eV.

Starting from four isolated vacancies, the ground state for the tetravacancy is reached in about 0.51 μs and 1482 KMC steps. The ground state is characterized by four vacancies

TABLE III. Relaxation volume (V^{rel}) and migration volume (in \AA^3) for pathways between the six dominant bound states for the divacancy complex.

To \ From	From					
	1NN	2NN	3NN	4NN	5NN	6NN
V^{rel}	-4.087	-5.684	-4.835	-5.301	-4.854	-5.111
1NN		0.964	-1.077		-0.639	
2NN	-2.562			-2.021		
3NN	-1.824			-1.180		
4NN		1.637	-1.646		-1.874	-1.687
5NN	-1.407			-1.428		
6NN				-1.498		

forming a complex of four 4NN and two 2NN vacancy-pair-separation distances. As measured from four isolated vacancies, the binding energy for the ground state is 1.36 or 0.34 eV per vacancy having a relaxation volume of -7.008\AA^3 . Table VI summarizes the energy landscape providing information regarding formation, and migration energies and Table VII represents the relaxation volume and migration volume for most 10 stable tetravacancies bound compounds. The dominant diffusion mechanism for the tetravacancy complex is described in Fig. 4. Diffusion takes place in two steps by the migration of one vacancy that jumps to 1NN position at each step. From the ground state, the system reaches a higher-energy state at 0.179 eV above the GS by crossing an energy barrier of 0.703 eV; from this state, a second barrier with an energy of 0.524 eV brings the system back into a new GS. The migration volume of the dominant diffusion mechanism is -4.909\AA^3 . The barrier height we find here agrees with the previous literature values using different empirical potentials (see Table I) [33].

D. Five-vacancy cluster

Having characterized the vacancies aggregation and diffusion mechanism of small vacancy clusters containing two to four vacancies, we now look at the energy landscape and diffusion mechanisms for five-vacancy clusters. The k-ART simulations are launched from line dislocation (LD) oriented

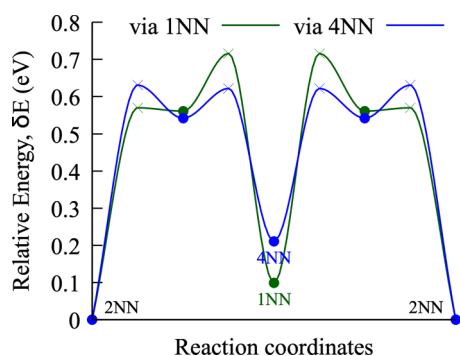


FIG. 5. Energetic descriptions of the migration between 2NN to 1NN (green) and 2NN to 4NN (blue) for divacancy. The cross and filled circle represent the saddle points and minima, respectively.

in three crystallographic orientations constructed by removing five atoms at [100], [110], and [111] directions, respectively, from the 2000-atom box. Each system is run for 5000 KMC steps, representing 21.8, 25.9, and 17.7 μs of simulation time at 600 K for $\text{LD}_{[100]}^5$, $\text{LD}_{[110]}^5$, and $\text{LDS}_{[111]}^5$, respectively, which allows the complete characterization of the dynamic evolution of these defects.

Figure 6 represents the cumulative topologies as a function of KMC step. At the end of the simulations for $\text{LD}_{[100]}^5$, $\text{LD}_{[110]}^5$, and $\text{LD}_{[111]}^5$ systems, 5122, 12 296, and 2923 topologies in total are analyzed for new events over 5000 KMC steps, respectively. Among these topologies, the number of unique topologies visited for $\text{LD}_{[100]}^5$, $\text{LD}_{[110]}^5$, and $\text{LD}_{[111]}^5$ are 219, 550, and 139, respectively. There are two main features of the cumulative topology plot, which can be described as the exploration of new topologies or oscillations between already encountered topologies. The exploration of new topologies is illustrated by the increase in cumulative topologies, where the simulation visits unexplored configurations. Plateaus on the topology curve indicate the recycling of topologies already encountered.

Figures 7 and 8 present the energy evolution and the detailed activation energy, binding energy at the local minima, and squared displacement as a function of time at 600 K, respectively. The selected and sampled activation energies as a function of KMC step, as well as the number of events in the catalog per step for events involving vacancy movement, are shown in Fig. S2 in the Supplemental Material [66]. As expected, the LD structure for the five vacancies is quite unstable and rapidly collapses into a five-vacancy bound complex irrespective of the initial orientation. The ground state (GS), composed of six 1NN, three 2NN, and one 3NN vacancy-pair-separation distance, is reached in about 2.3 μs (1519 KMC steps), 1.8 μs (1935 KMC steps), and 3.1 μs (1789 KMC steps) for $\text{LD}_{[100]}^5$, $\text{LD}_{[110]}^5$, and $\text{LD}_{[111]}^5$, respectively. Therefore, the initial $\text{LD}_{[100]}^5$, $\text{LD}_{[110]}^5$, and $\text{LD}_{[111]}^5$ structures are 0.78, 1.83, and 1.16 eV, respectively, above the GS. Going back to the initial LD structure, the system would need to cross significant effective barriers of 2.13, 2.44, and 1.75 eV, respectively, as measured from the ground state. The collapse of all three LD structures occurs in the same manner, triggered by one atom entering at the corner of the LD structure, requiring an activation barrier of 0.630, 0.607, and 0.595 eV for $\text{LD}_{[100]}^5$, $\text{LD}_{[110]}^5$, and $\text{LD}_{[111]}^5$ respectively. The first few steps of the collapse for each of the three LD structures are shown in Fig. S3 in the Supplemental Material [66].

Once vacancies reach the ground state, 10 configurations dominate the dynamics of the system, representing more than 90% of all accepted configurations. Table VIII summarizes the energy landscape providing information regarding formation and transition energies and Table IX represents the relaxation volume and migration volume for the 10 most stable pentavacancy bound compounds. Figure 9 represents the three most dominant diffusion mechanisms denoted as M_1 , M_2 , and M_3 for this complex. Mechanism M_1 is completed going through one intermediate state. From the ground state, the system moves to a bound state (0.129 eV above the GS), with a composition of four 1NN, four 2NN, and two 3NN vacancy-pair-separation distances by crossing an activation barrier of

TABLE IV. Formation energy (E_{nv}^F) and migration energies (in eV) for pathways between the eight dominant bound states for the trivacancy complex. The bound structures of the trivacancy complex are defined as $3V(N_{d_1}, N_{d_2}, N_{d_3}, N_{d_4}, N_{d_5}, N_{d_6})$, where $N_{d_1}, N_{d_2}, N_{d_3}, N_{d_4}, N_{d_5}$, and N_{d_6} represent the total number of 1NN, 2NN, 3NN, 4NN, 5NN, and 6NN vacancy-pair-separation distances, respectively.

From To	3V (2,1,0,0,0,0)	3V (0,2,0,0,0,1)	3V (0,2,1,0,0,0)	3V (1,1,0,1,0,0)	3V (0,1,0,2,0,0)	3V (1,0,0,1,1,0)	3V (0,0,0,2,1,0)	3V (0,0,1,2,0,0)
E_{nv}^F	4.625	4.685	4.709	4.780	4.867	5.031	5.127	5.128
3V (2,1,0,0,0,0)	0.653		0.605	0.475		0.364		
3V (0,2,0,0,0,1)								
3V (0,2,1,0,0,0)	0.691			0.60	0.461			0.233
3V (1,1,0,1,0,0)	0.631		0.671		0.521			
3V (0,1,0,2,0,0)			0.619	0.608			0.380	0.415
3V (1,0,0,1,1,0)	0.773							
3V (0,0,0,2,1,0)					0.640			
3V (0,0,1,2,0,0)			0.653		0.676			

0.638 eV, followed up with a transition of 0.509 eV system move to the new GS to complete the migration. Mechanism M_2 is symmetrical and visits two intermediate bound configurations. From the ground state, the system moves to the bound state (0.211 eV above the GS), which has a composition of five 1NN, three 2NN, one 3NN, and one 4NN vacancy-pair-separation distances, crossing a 0.740-eV, then a 0.513-eV barrier, to bring the system into a new intermediate bound state with the same structure. Finally, the system reaches a translated GS by crossing a 0.528-eV barrier. Like M_2 , mechanism M_3 is also symmetrical and is completed through four intermediate bound states having an overall migration barrier of 0.937 eV. The migration volumes of the mechanism M_1 , M_2 and M_3 are -6.570 , -5.208 , and -6.743 \AA^3 , respectively.

E. Eight-vacancy cluster

To see how the collapse of the line dislocation (LD) structure occurs as the LD size increases, we analyze the LD structure containing eight vacancies along [100], [110], and [111] directions. These systems are run for 7000 KMC steps representing 280, 250, and 122 μs of simulation time for $\text{LD}_{[100]}$, $\text{LD}_{[110]}$, and $\text{LD}_{[111]}$, respectively at 600 K. At the end of the simulations, around 6202, 7331, and 6347 topologies have been analyzed for new events for $\text{LD}_{[100]}$, $\text{LD}_{[110]}$, and $\text{LD}_{[111]}$, respectively. Among these, the number of unique topologies visited, i.e., selected during the kinetics,

for $\text{LD}_{[100]}^5$, $\text{LD}_{[110]}^5$ and $\text{LD}_{[111]}^5$, are 298, 332, and 253, respectively. Figure 10 plots the energy evolution and Fig. 11 the detailed activation energy, binding energy at the local minima, and squared displacement as a function of time at 600 K. The selected and sampled activation energies as a function of the KMC step, as well as the number of events in the catalog per step for events involving vacancy movement, are shown in Fig. S4 in the Supplemental Material [66]. As for the five-vacancy LDs, the structures collapse into an eight-vacancy bound compact complex, but over a timescale 2 to 10 times longer: The ground state (GS) is reached in about 53.9 μs (2566 KMC steps), 112.8 μs (5132 KMC steps), and 0.2 μs (663 KMC steps) for $\text{LD}_{[100]}$, $\text{LD}_{[110]}$, and $\text{LD}_{[111]}$, respectively. This is accompanied by a relaxation of 2.45, 4.25, and 3.12 eV, respectively, from the initial $\text{LD}_{[100]}$, $\text{LD}_{[110]}$, and $\text{LD}_{[111]}$ structures. Going back to the initial LD structure, the system must cross significant effective barriers of 3.69, 5.02, and 3.85 eV, respectively, as measured from the ground state.

The ground state of the eight-vacancy cluster has a combination of twelve 1NN, eight 2NN, four 3NN, and four 4NN vacancy-pair-separation distances. This cluster is characterized by a binding energy of 4.139 eV (0.517 eV per vacancy). While a large number of states are accessed during the simulation, three actual diffusion events take place after the bound complex is formed. Including various oscillations, mechanism M_1 takes place over 74 KMC steps over 1 μs , mechanism M_2 takes place over 376 KMC steps over 4.9 μs , and mechanism

TABLE V. Relaxation volume (V^{rel}) and migration volume (in \AA^3) for pathways between the eight dominant bound states for the trivacancy complex. The bound structures of the trivacancy complex are defined as $3V(N_{d_1}, N_{d_2}, N_{d_3}, N_{d_4}, N_{d_5}, N_{d_6})$, where $N_{d_1}, N_{d_2}, N_{d_3}, N_{d_4}, N_{d_5}$, and N_{d_6} represent the total number of 1NN, 2NN, 3NN, 4NN, 5NN, and 6NN vacancy-pair separation distances, respectively.

From To	3V (2,1,0,0,0,0)	3V (0,2,0,0,0,1)	3V (0,2,1,0,0,0)	3V (1,1,0,1,0,0)	3V (0,1,0,2,0,0)	3V (1,0,0,1,1,0)	3V (0,0,0,2,1,0)	3V (0,0,1,2,0,0)
V^{rel}	-6.264	-8.957	-8.702	-7.353	-8.744	-6.521	-7.880	-7.830
3V (2,1,0,0,0,0)	-1.920		-1.105	-1.574		-0.953		
3V (0,2,0,0,0,1)								
3V (0,2,1,0,0,0)	-3.542			-2.667	-1.731			-2.244
3V (1,1,0,1,0,0)	-2.663		-1.319		-1.284			
3V (0,1,0,2,0,0)			-1.774	-2.67			-2.210	-2.068
3V (1,0,0,1,1,0)	-1.210							
3V (0,0,0,2,1,0)					-1.344			
3V (0,0,1,2,0,0)			-1.372		-1.153			

TABLE VI. Formation energy (E_{nv}^F) and migration energies (in eV) for pathways between the 10 dominant bound states for the tetravacancy complex. The bound structures of the tetravacancy complex are defined as $4V(N_{d_1}, N_{d_2}, N_{d_3}, N_{d_4}, N_{d_5}, N_{d_6})$, where $N_{d_1}, N_{d_2}, N_{d_3}, N_{d_4}, N_{d_5}$, and N_{d_6} represent the total number of 1NN, 2NN, 3NN, 4NN, 5NN, and 6NN vacancy-pair-separation distances, respectively.

From To	4V (4,2,0,0,0,0)	4V (3,2,1,0,0,0)	4V (3,2,0,1,0,0)	4V (4,1,1,0,0,0)	4V (2,2,0,2,0,0)	4V (2,2,1,1,0,0)	4V (3,1,0,1,1,0)	4V (3,1,1,1,0,0)	4V (1,2,1,2,0,0)	4V (2,1,1,1,1,0)
E_{nv}^F	5.763	5.942	5.945	6.014	6.093	6.127	6.195	6.196	6.262	6.376
4V (4,2,0,0,0,0)		0.524		0.555		0.410				0.376
4V (3,2,1,0,0,0)	0.703		0.483	0.407	0.498			0.272		
4V (3,2,0,1,0,0)		0.485				0.478			0.373	
4V (4,1,1,0,0,0)	0.804	0.479								0.284
4V (2,2,0,2,0,0)		0.648							0.432	
4V (2,2,1,1,0,0)	0.773		0.660			0.511	0.595			
4V (3,1,0,1,1,0)						0.664				0.389
4V (3,1,1,1,0,0)		0.525								0.318
4V (1,2,1,2,0,0)			0.690		0.619				0.377	
4V (2,1,1,1,1,0)	0.988			0.654			0.570	0.499		0.318

M_3 takes place over 423 KMC steps over 21.5 μs . Reducing the process to its essential steps, the diffusion mechanisms M_1, M_2 , and M_3 for the eight-vacancy cluster can be reduced to 6, 13, and 25 jumps, respectively, as shown in Fig. 12. For the mechanisms, M_1, M_2 , and M_3 , the migration energy (migration volume) over pathways connecting ground states is 1.093 eV (-2.907 \AA^3), 1.271 eV (-4.623 \AA^3), and 1.30 eV (-2.964 \AA^3), respectively, with M_1 being the most probable diffusion mechanism at 600 K.

E. Lifetime and diffusion coefficients of vacancy cluster

The average thermal lifetime and diffusion coefficient for the various clusters are listed in Table X. Both the two- and three-vacancy clusters have diffusion coefficients on the same order of magnitude as a single vacancy, with $4.7 \times 10^8 \text{ \AA}^2 \text{ s}^{-1}$ and $4.7 \times 10^8 \text{ \AA}^2 \text{ s}^{-1}$, respectively. The average thermal lifetimes for the two- and three-vacancy clusters are 0.036 and 0.2 μs , respectively. The bound two- and three-vacancy cluster compounds diffuse for an average of 24 and 224 steps, respectively, before dissociating. Further increasing the number of vacancies in the cluster (four- and five-vacancy clusters) significantly decreases the diffusion coefficient. The

diffusion coefficient of four- and five-vacancy clusters is one and three orders of magnitude lower than that of a single vacancy, respectively: $1.1 \times 10^7 \text{ \AA}^2 \text{ s}^{-1}$ and $9 \times 10^5 \text{ \AA}^2 \text{ s}^{-1}$. Their lifetimes at 600 K are 3 and 13 μs , respectively. The bound clusters of four and five vacancies diffuse on average 122 and 145 steps, respectively, before dissociating. Even a cluster of eight vacancies can be mobile with a diffusion coefficient of $1.8 \times 10^4 \text{ \AA}^2 \text{ s}^{-1}$ associated with a relatively high migration energy ($>1 \text{ eV}$). Our results regarding the average thermal lifetime are qualitatively consistent with those of previous experiments [67–69]. Larger vacancy clusters have longer thermal lifetimes, which contributes to the kinetic stabilization of vacancy clusters. However, there are quantitative discrepancies between our results and experimentally determined lifetimes. These discrepancies arise from the fact that the criteria for sinking and temperature are different.

G. Relations between migration barriers, minimum energies, and migration volumes

The correlation between migration energy, minimum energy, and migration volume for vacancy clusters with two

TABLE VII. Relaxation volume (V^{rel}) and migration volume (in \AA^3) for pathways between the 10 dominant bound states for the tetravacancy complex. The bound structures of the tetravacancy complex are defined as $4V(N_{d_1}, N_{d_2}, N_{d_3}, N_{d_4}, N_{d_5}, N_{d_6})$, where $N_{d_1}, N_{d_2}, N_{d_3}, N_{d_4}, N_{d_5}$, and N_{d_6} represent the total number of 1NN, 2NN, 3NN, 4NN, 5NN, and 6NN vacancy-pair-separation distances, respectively.

From To	4V (4,2,0,0,0,0)	4V (3,2,1,0,0,0)	4V (3,2,0,1,0,0)	4V (4,1,1,0,0,0)	4V (2,2,0,2,0,0)	4V (2,2,1,1,0,0)	4V (3,1,0,1,1,0)	4V (3,1,1,1,0,0)	4V (1,2,1,2,0,0)	4V (2,1,1,1,1,0)
V^{rel}	-7.008	-8.352	-8.427	-6.910	-9.612	-9.30	-7.958	-7.830	-10.650	-8.456
4V (4,2,0,0,0,0)		-3.565		-6.737		-1.351				-0.256
4V (3,2,1,0,0,0)	-4.909		-4.163	-6.662	-1.217			-4.440		
4V (3,2,0,1,0,0)		-4.237				-3.453			-1.661	
4V (4,1,1,0,0,0)	-6.639	-4.166								?
4V (2,2,0,2,0,0)		-2.477							-1.701	
4V (2,2,1,1,0,0)	-3.643		-4.324			-5.993	-2.728			
4V (3,1,0,1,1,0)						-1.386				-3.328
4V (3,1,1,1,0,0)		-3.918								-3.784
4V (1,2,1,2,0,0)			-3.885		-2.739				-2.992	
4V (2,1,1,1,1,0)	-1.704						-3.826	-4.410		-4.251

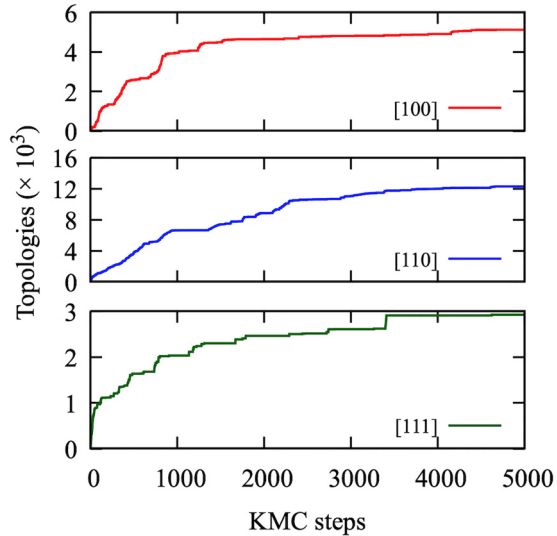


FIG. 6. Evolution of the number of topologies as a function of KMC steps for initial line dislocation contains five vacancies along [100] (top), [110] (middle), and [111] (bottom).

to five vacancies is shown in Fig. 13. The plots in the left column show the migration energy as a function of the energy at the local minima measure with respect to the ground state. We observe a noisy but clear correlation, with the migration energy decreasing with higher-energy minima. This correlation can be explained by the fact that a strong local deformation increases the local energy mainly by weakening the interactions. Additional information about the physics behind the barriers is obtained by plotting the migration energy as a function of migration volume. Here, however, we do not observe significant correlation between the migration volume and the diffusion barriers. This suggests that the elastic deformation that leads to the correlation found in the left-column graphs is not dominated by local volume expansion or contraction but involves more complex bounding terms.

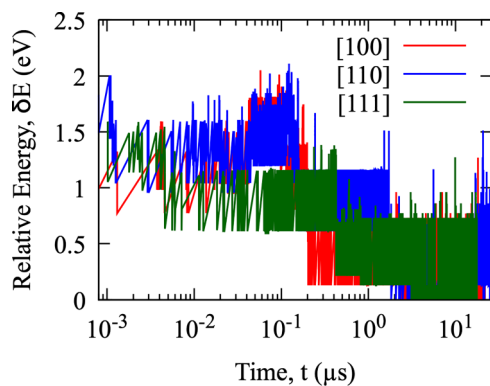


FIG. 7. Energy evolution of five vacancies as a function of time at 600 K: Red, blue, and green lines for initial line dislocation structures along [100], [110], and [111], respectively.

IV. DISCUSSION

The kinetics of vacancies plays an essential role in determining the properties of a material. Understanding the aggregation and diffusion mechanisms of vacancies is therefore a crucial step in further exploring the mechanical and electrical properties of structural materials associated with the formation of vacancies by deformation or radiation [70–74]. However, experimental approaches are generally unable to provide the required detailed microscopic information that would allow us to fully understand this role. Direct calculations can compensate for experimental limitations in the case of simple point defects, but the rapidly increasing complexity of the energy landscape of even small clusters requires automated search tools such as the kinetic activation-relaxation technique (k-ART).

Accessing large timescale and system sizes, k-ART simulations presented here provide a detailed characterization of vacancy aggregation and clustering diffusion processes and the associated energy landscapes, showing a relatively complex picture even for the simplest systems. This picture is well characterized with k-ART since the catalog is updated and expanded at every step as new topologies are explored.

We analyze the energy landscape associated with bcc crystalline Fe containing one to eight vacancies. The more complete energy landscape generated here and obtained with simulations that reached several hundred microseconds allows us to identify new mechanisms. Comparison with previously published works [19,42] for the monovacancy diffusion, using EAM force fields, confirms that the correct basic diffusion mechanisms are recovered for this system. For small vacancy cluster diffusion with two to four defects, the mechanisms predicted and diffusivity trends match those seen in the literature [17–19,33]. For divacancy, a global minimum energy with a $V-V$ distance separation of the second-nearest neighbor (2NN) is found, in agreement with previous MD and DFT studies. The mechanism of migration of the divacancy in iron consists of an oscillation not only between 2NN and 1NN states but also, largely, between 2NN and 4NN states, even though the 1NN state is strongly bound compared to the 4NN state. These thermodynamically counterintuitive diffusion mechanisms of divacancy could easily be misidentified when using simpler approaches, e.g., the nudged elastic band method (NEBM). Although these mechanisms have been captured with traditional KMC and careful analysis of DFT results [17], here they arise naturally without any special consideration or bias. For trivacancy cluster, the migration energy of the dominant diffusion mechanism is 0.64 eV, very close to the diffusion barrier for monovacancy. Previously, using DFT-NEBM, Fu *et al.* [19] obtained an activation energy of 0.35 eV lower than the value that we find here; however, the general mechanism matches the one presented here. However, Kandaskalov *et al.* [18] repeated the DFT study and reported results of two types of numerical simulations: In the first simulation, the Fe atom is fixed between the two nearest vacancies, and in the second simulation, it is placed in the center of a four-vacancy. In the first case, the mechanism obtained, with a 0.64-eV barrier, matches the mechanism found here while the second simulation leads to a 0.36-eV barrier that has not been generated here, even with additional ARTn searches.

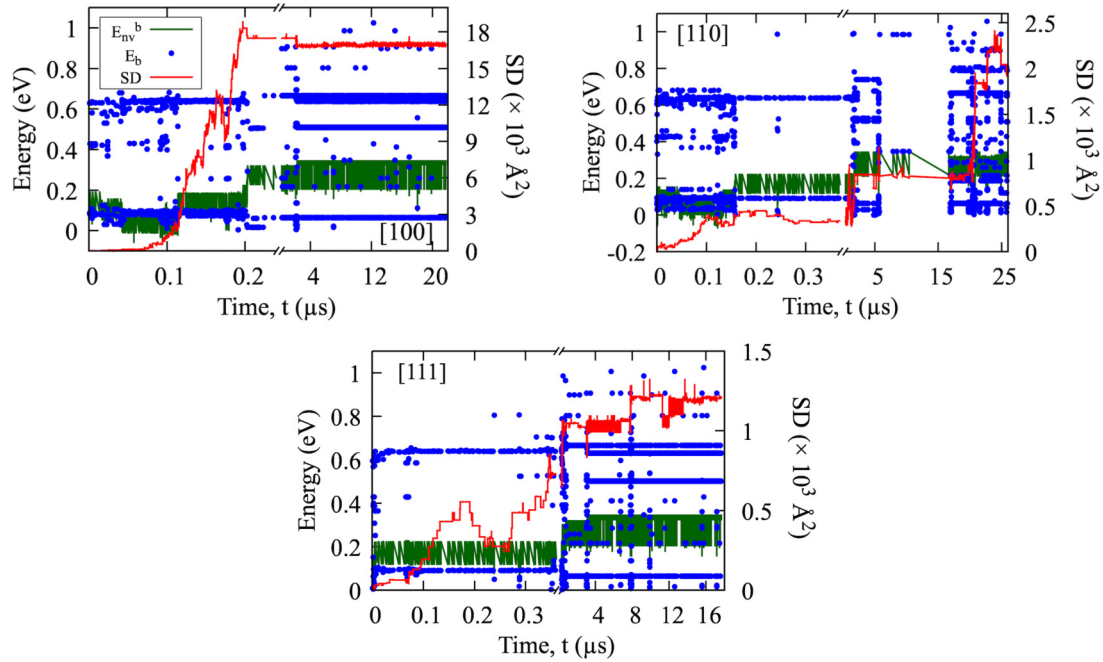


FIG. 8. Activation-energy (left, blue symbols), binding energy at the local minima (left, green line), and squared displacement (right, red line) as a function of time for the line dislocation of five vacancies along [100] (top left), [110] (top right), and [111] (bottom center) direction in a bcc Fe at 600 K.

Looking at the tetravacancy, we find that the dominant mechanism has a 0.703-eV barrier, a little higher than the values found in previous DFT calculations [18,19]. This could be due to image interactions introduced by the small unit-cell supercell used or to accuracy issues with the EAM potential. A recent DFT work, however, indicates significant finite-size effects affecting the height of the calculated energy barriers [75]. Nevertheless, the match in the mechanism pathway is reassuring and indicates the key physics is being captured by the potential. The barrier height we find here agrees with the previous literature value using different empirical potentials [33]. Furthermore, during simulation, we find that degenerate or quasidegenerate saddle points are not so rare. These states play an essential role in cluster diffusion. Even though larger

vacancy clusters are less mobile, they can still move, and we identified diffusion mechanisms for five- and eight-vacancy clusters.

To understand the effects of stress on diffusion, we analyze the elastic dipole tensors and relaxation volume tensors at both equilibrium and the saddle point, while also examining the migration volume along diffusion pathways for vacancy clusters.

Table XI summarizes the elastic dipole and relaxation volume tensor in both the equilibrium and transition states highlighting the migration volume along the $[11\bar{1}]$ direction for monovacancy. In agreement with previous DFT results of Ma *et al.* [61], we also observe a negative migration volume for monovacancy in α -iron. The value of migration volume

TABLE VIII. Formation energy (E_{nv}^F) and migration energies (in eV) for pathways between the 10 dominant bound states for the pentavacancy complex. The bound structures of the pentavacancy complex are defined as $5V(N_{d_1}, N_{d_2}, N_{d_3}, N_{d_4}, N_{d_5}, N_{d_6})$, where $N_{d_1}, N_{d_2}, N_{d_3}, N_{d_4}, N_{d_5}$, and N_{d_6} represent the total number of 1NN, 2NN, 3NN, 4NN, 5NN, and 6NN vacancy-pair-separation distances, respectively.

From To	5V (6,3,1,0,0,0)	5V (4,4,2,0,0,0)	5V (5,3,1,1,0,0)	5V (4,3,0,2,0,1)	5V (4,3,2,0,1,0)	5V (4,3,1,2,0,0)	5V (5,2,2,1,0,0)	5V (3,3,3,1,0,0)	5V (4,2,2,2,0,0)	5V (0,5,4,0,1,0)
E_{nv}^F	6.873	7.002	7.084	7.234	7.257	7.258	7.333	7.468	7.497	7.509
5V (6,3,1,0,0,0)		0.509	0.528				0.348	0.429		
5V (4,4,2,0,0,0)	0.638		0.803		0.293				0.412	0.480
5V (5,3,1,1,0,0)	0.740			0.513	0.501	0.621	0.477	0.363	0.381	
5V (4,3,0,2,0,1)				0.651			0.623			
5V (4,3,2,0,1,0)							0.477			0.574
5V (4,3,1,2,0,0)		0.548	0.795				0.429		0.362	
5V (5,2,2,1,0,0)	0.808		0.726	0.723	0.552	0.504		0.590	0.268	
5V (3,3,3,1,0,0)	1.024		0.748				0.725			
5V (4,2,2,2,0,0)		0.906	0.794			0.601	0.432			
5V (0,5,4,0,1,0)		0.987			0.826					

TABLE IX. Relaxation volume (V^{rel}) and migration volume (in \AA^3) for pathways between the 10 dominant bound states for the pentavacancy complex. The bound structures of the pentavacancy complex are defined as $5V(N_{d_1}, N_{d_2}, N_{d_3}, N_{d_4}, N_{d_5}, N_{d_6})$, where $N_{d_1}, N_{d_2}, N_{d_3}, N_{d_4}, N_{d_5}$, and N_{d_6} represent the total number of 1NN, 2NN, 3NN, 4NN, 5NN, and 6NN vacancy-pair-separation distances, respectively.

From To	5V (6,3,1,0,0,0)	5V (4,4,2,0,0,0)	5V (5,3,1,1,0,0)	5V (4,3,0,2,0,1)	5V (4,3,2,0,1,0)	5V (4,3,1,2,0,0)	5V (5,2,2,1,0,0)	5V (3,3,3,1,0,0)	5V (4,2,2,2,0,0)	5V (0,5,4,0,1,0)
V^{rel}	-7.943	-11.015	-9.078	-10.434	-10.508	-10.629	-8.968	-11.291	-10.202	-15.325
5V (6,3,1,0,0,0)		-3.119	-4.072				-3.647	-0.824		
5V (4,4,2,0,0,0)	-6.570		-10.541			-4.390			-8.226	0.106
5V (5,3,1,1,0,0)	-5.208			-4.153	-1.163	-5.590	-5.718	-3.005	-6.032	
5V (4,3,0,2,0,1)					-2.519		-2.152			
5V (4,3,2,0,1,0)							-3.402			-0.35
5V (4,3,1,2,0,0)		-4.004	-7.141				-6.766		-4.177	
5V (5,2,2,1,0,0)	-4.672		-5.608	-0.686	-3.694	-5.109		-1.546	-5.765	
5V (3,3,3,1,0,0)	-4.172			-5.219				-3.869		
5V (4,2,2,2,0,0)		-7.413	-7.156			-3.750		-6.999		
5V (0,5,4,0,1,0)		-4.204			-5.167					

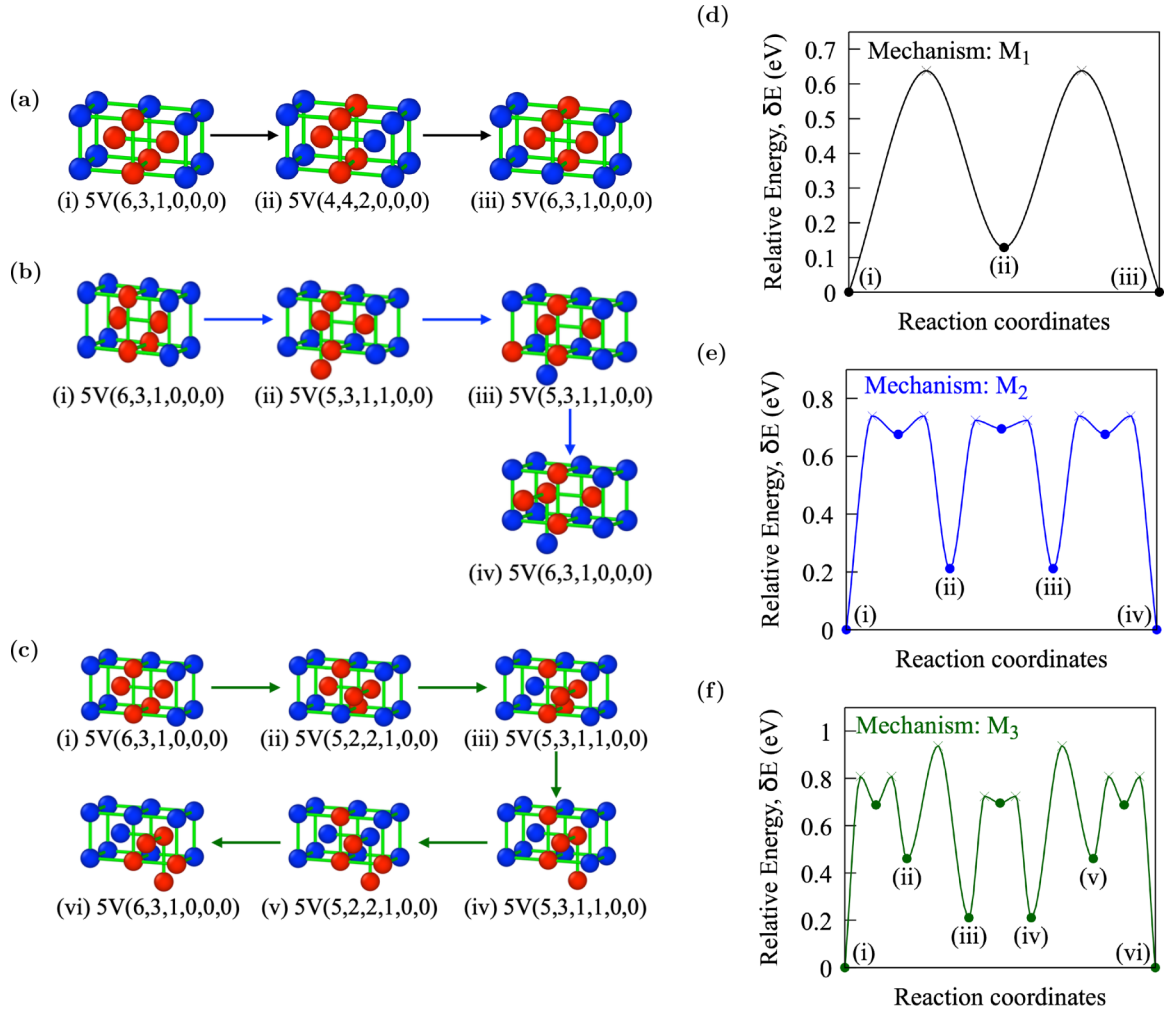


FIG. 9. Schematic representations of diffusion pathways (a)–(c) and corresponding energetic evolution (d)–(f) for the three most dominant diffusion mechanisms M_1 , M_2 , and M_3 , respectively associated with the five-vacancy cluster in bcc Fe at 600 K. In the schematic diagrams, the blue and red spheres represent crystalline Fe atoms and vacancies, respectively. The cross and filled circles on the energetic graphs represent the saddle points and minima, respectively. Indices (I, II, III, etc.) are used to identify states and explain the diffusion mechanism. The bound structures are defined as $5V(N_{d_1}, N_{d_2}, N_{d_3}, N_{d_4}, N_{d_5}, N_{d_6})$, where $N_{d_1}, N_{d_2}, N_{d_3}, N_{d_4}, N_{d_5}$, and N_{d_6} represent the total number of 1NN, 2NN, 3NN, 4NN, 5NN, and 6NN vacancy-pair-separation distances, respectively.

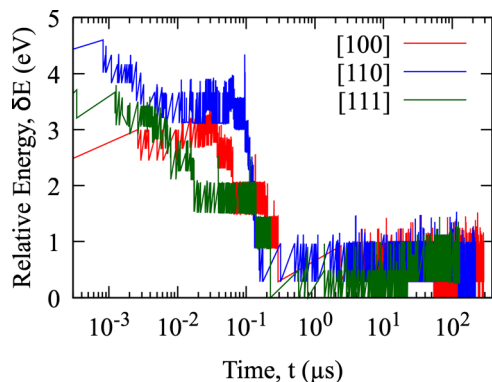


FIG. 10. Energy evolution of eight vacancies as a function of time at 600 K: Red, blue, and green lines for the initial line dislocation structures along [100], [110], and [111], respectively.

found in our study is slightly smaller than that of Ref. [61]: Our calculations yield a migration volume of -1.625 \AA^3 for monovacancy in Fe, while Ma *et al.* obtained -0.238 \AA^3 . This discrepancy is primarily due to different lattice parameters: Ma *et al.* [61,76] assumed an equilibrium lattice parameter of 2.831 \AA , whereas our fixed volume calculations assume 2.8553 \AA . A negative migration volume indicates a decrease in migration energy and an increase in the diffusion coefficient during hydrostatic compression. Figure 14 shows monovacancy migration energies and diffusion coefficients change with pressure at a temperature of 600 K. With increasing pressure from 0 to 12 kbar, monovacancy migration energy decreases by 0.012 eV, while the diffusion coefficient

increases by $2.94 \times 10^{-15} \text{ m}^2 \text{ s}^{-1}$. Conversely, during lattice expansion with negative pressure from 0 to 12 kbar, migration energy increases by 0.013 eV, and diffusion coefficient decreases by $2.44 \times 10^{-15} \text{ m}^2 \text{ s}^{-1}$.

Moreover, we find that the off-diagonal elements of the elastic dipole and the relaxation volume tensor for vacancies are zero at equilibrium and change to nonzero values at the saddle point along the diffusion paths. The results are similar to those found with DFT calculations [61,76,77] and molecular statics [78], indicating that the applied shear stress may have a significant effect on vacancy diffusion as variations in migration barriers caused by external stress interactions can lead to directional differences and anisotropic diffusion. Furthermore, for vacancy clusters, we find no clear trend in the variation of migration volume for the identified dominant pathways (Table III, V, VII, IX), suggesting that pressure effects on transition states finely depend on the local environment (see Fig. 15).

In summary, the presence of external stresses or local stress fields resulting from extended defects can increase the complexity of vacancy cluster diffusion. These conditions may favor mechanisms that may be neglected in analyses with a limited viewpoint, ultimately exerting a substantial influence on the overall material properties.

V. CONCLUSION

Using the kinetic activation-relaxation technique (k-ART) coupled with an embedded-atom method (EAM) potential, we study the vacancy aggregation and clustering diffusion processes in α -Fe. Our results show a richness in the diffusion

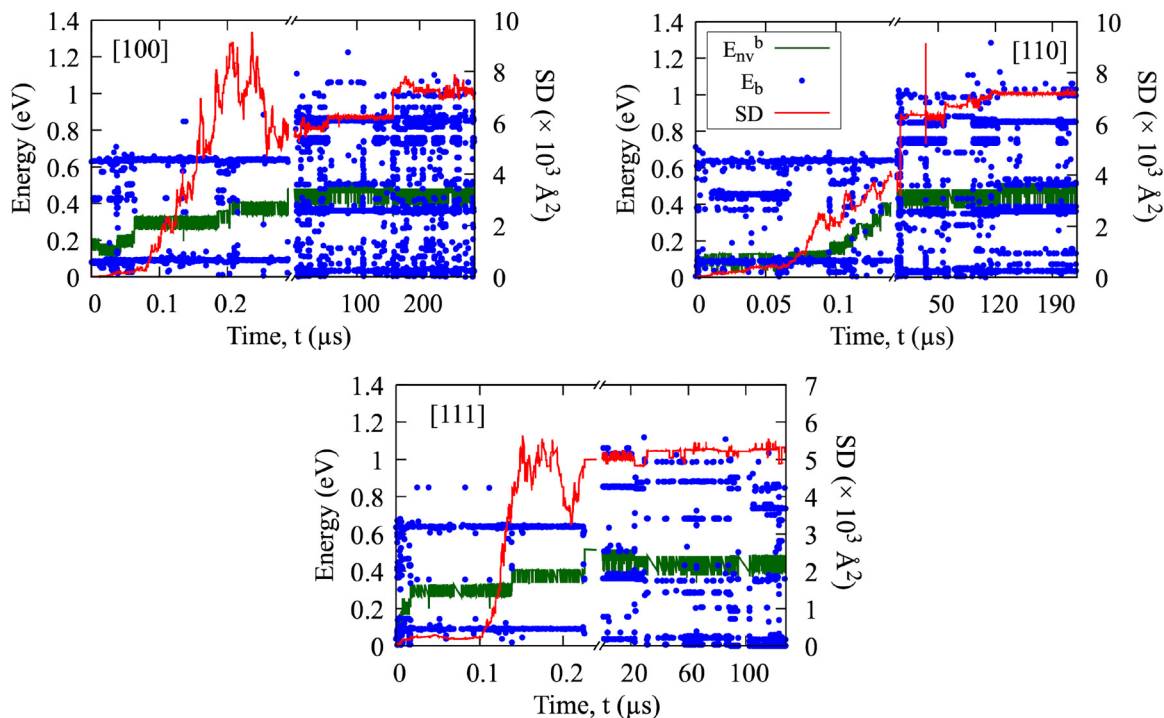


FIG. 11. Activation-energy (left, blue symbols), binding energy at the local minima (left, green line), and squared displacement (right, redline) as a function of time for the line dislocation of eight vacancies along [100] (top left), [110] (top right), and [111] (bottom center) direction in a bcc Fe at 600 K.

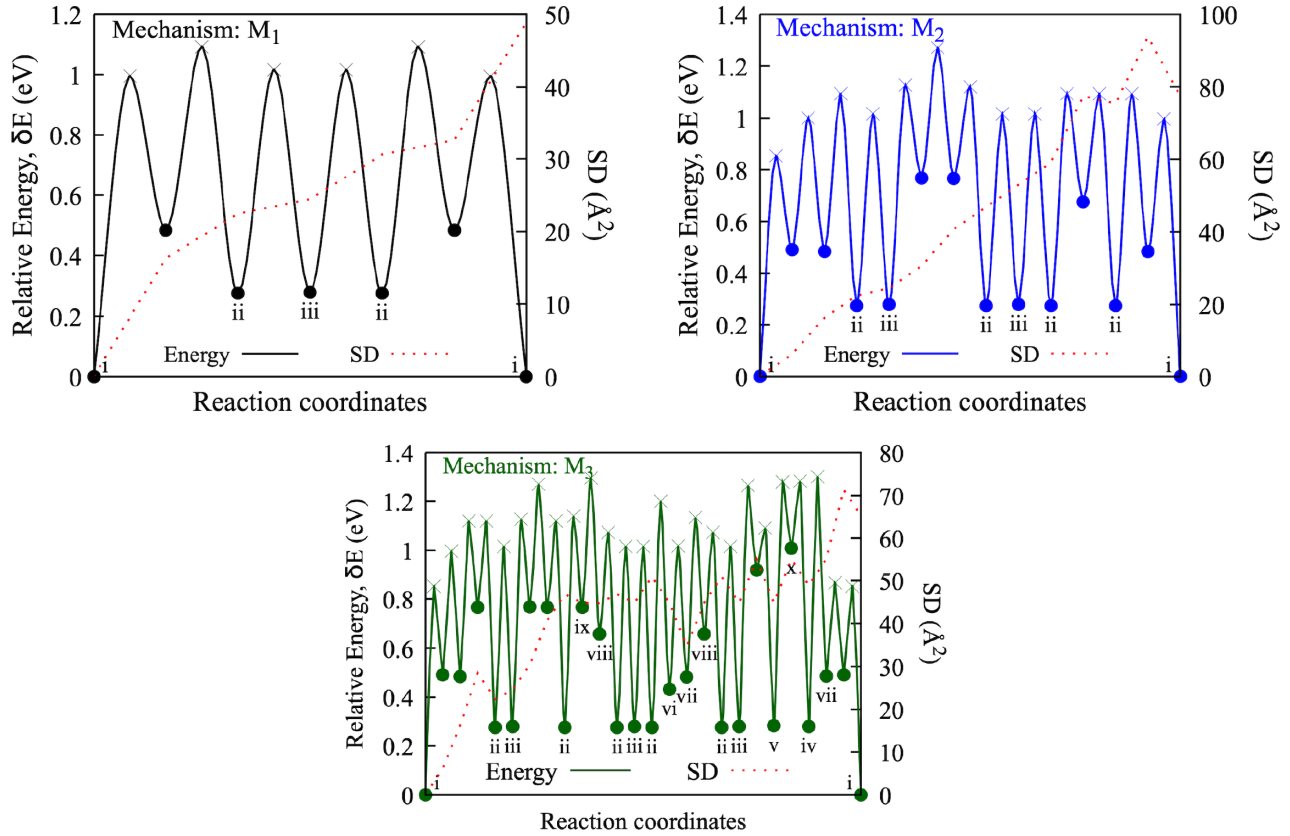


FIG. 12. Energy barriers and square displacement for the diffusion mechanism (ground state to ground state) of eight-vacancy cluster. Numeric numbers (i to x) represent the bound states, where (i) $8V(12, 8, 4, 4, 0, 0)$, (ii) $8V(12, 7, 5, 3, 1, 0)$, (iii) $8V(12, 7, 5, 4, 0, 0)$, (iv) $8V(12, 7, 4, 4, 1, 0)$, (v) $8V(12, 7, 4, 4, 0, 1)$, (vi) $8V(10, 8, 6, 2, 2, 0)$, (vii) $8V(11, 7, 5, 4, 1, 0)$, (viii) $8V(10, 7, 4, 6, 0, 1)$, (ix) $8V(11, 6, 4, 5, 1, 1)$, and (x) $8V(10, 6, 4, 5, 2, 1)$.

mechanisms as well as a complex balance between elastic and chemical effects. By reaching physically relevant timescales without presuppositions regarding mechanisms and elastic effects, this approach provides a detailed and reliable representation of the migration pathways of vacancy clusters, including rare pathways that are orders of magnitude less likely to occur in pure Fe than the dominant ones.

We find that the diffusion barriers of vacancies do not change monotonically with cluster size. Moreover, the number of possible barriers is much larger than previously identified. Even focusing on the barriers relevant at 600 K, we find considerable complexity that prevents the use of simplistic diffusion models. Degenerate or quasidegenerate saddle

points, for example, are much more common than generally thought. As discussed, these states play a significant role in cluster diffusion. As for the diffusion coefficient, we find that divacancies and trivacancies diffuse on the same order of magnitude as monovacancies. The stabilization of vacancy clusters is achieved both by energetics, with larger vacancy clusters having lower energy, and by kinetics: The thermal lifetime of vacancy clusters increases with cluster size. Yes, these larger clusters are less likely to interact with each other, as their diffusion coefficient decreases significantly with size.

Overall, these results provide a much deeper understanding of the microscopic and kinetic picture of vacancy clusters in α -Fe, a qualitative understanding that should be valid for all bcc metals. The complex energetic environment controlling the kinetics of small vacancy clusters presented here demonstrates that simple rules are not sufficient to develop a robust approach to predictive control and prevention of damage processes associated with vacancy clusters in structural metals. More work is needed to better characterize this behavior and derive general rules. It is clear that additional simulations are needed to capture the energy landscape of vacancy cluster diffusion in other materials or the presence of strains, defects, or impurities; simulations to this end are underway.

Previous work [79] indicates that the presence of vacancies decreases the Curie temperature of a system; however,

TABLE X. Average cluster lifetimes and diffusion coefficients for different vacancies at 600 K.

Cluster	Average thermal lifetime (s)	Diffusion coefficient ($\text{\AA}^2 \text{s}^{-1}$)
1V		7.17×10^8
2V	$(3.6 \pm 0.01) \times 10^{-8}$	$(4.7 \pm 0.01) \times 10^8$
3V	$(2.0 \pm 0.01) \times 10^{-7}$	$(2.2 \pm 0.01) \times 10^8$
4V	$(3.0 \pm 0.01) \times 10^{-6}$	$(1.1 \pm 0.02) \times 10^7$
5V	$(1.3 \pm 0.01) \times 10^{-5}$	$(9.0 \pm 0.04) \times 10^5$
8V		1.8×10^4

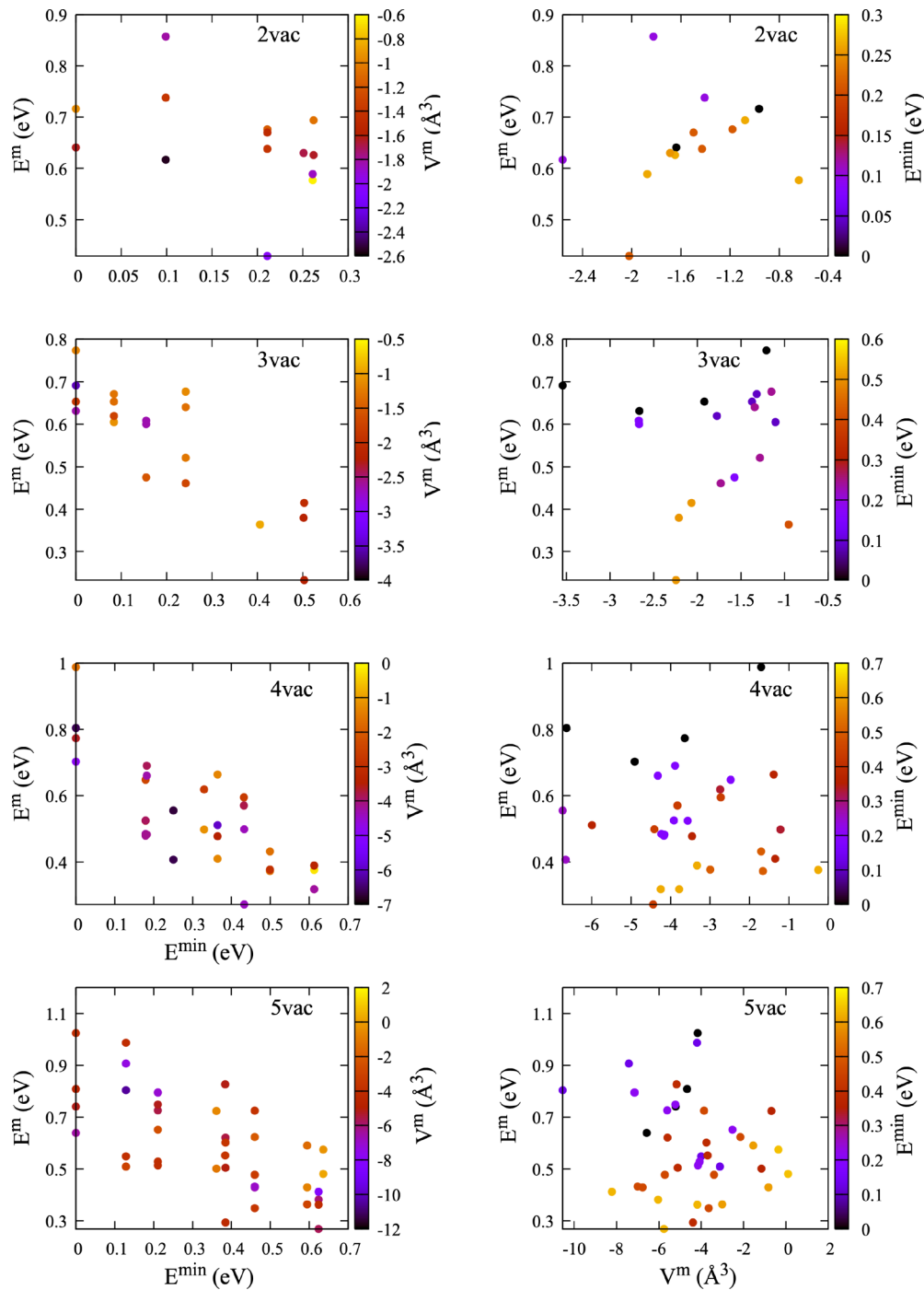


FIG. 13. Left: Relation between the energy minimum E^{\min} and the migration energy E^m ; right: Migration energy versus migration volume V^m for the same events. From top to bottom, the panels present data for most stable bound configurations two vacancies (listed in Table II) (top line), three vacancies (listed in Table IV) (second line), four vacancies (listed in Table VI) (third line), and five vacancies (listed in Table VIII) (bottom line).

magnetic moments increase in the vicinity of vacancies. More work is therefore needed to fully understand how these bound vacancy clusters influence the magnetic properties of bulk iron. As large simulation box sizes are needed to limit self-interactions for these complex configurations, calculating these properties is, however, a significant project in itself.

In summary, if the use of empirical potential limits the general application to defect kinetics, the agreement with DFT

calculations for some of the simpler mechanisms suggests that the main results presented here are physically relevant. On a qualitative level, these show that complex diffusion mechanisms can be important even in systems as simple as the one presented here. Recovering dominant diffusion, but also trapping mechanisms (for instance, the transition between 2NN state to 1NN state for divacancy cluster), requires much more than the simple identification of a few configurations by

TABLE XI. Elastic dipole tensor P_{ij} (in eV), relaxation volume tensor V_{ij} (in \AA^3) of both ground state (GS) and transition states (TS), and migration volume V^m (in \AA^3) along the $[11\bar{1}]$ direction for monovacancy in bcc iron.

	P_{ij} (in eV)	V_{ij} (in \AA^3)	V^m (in \AA^3)
GS	$\begin{pmatrix} -2.808 & 0 & 0 \\ 0 & -2.808 & 0 \\ 0 & 0 & -2.808 \end{pmatrix}$	$\begin{pmatrix} -0.843 & 0 & 0 \\ 0 & -0.843 & 0 \\ 0 & 0 & -0.843 \end{pmatrix}$	-1.625
TS	$\begin{pmatrix} -4.60 & -1.802 & 1.802 \\ -1.802 & -4.60 & 1.802 \\ 1.802 & 1.802 & -4.60 \end{pmatrix}$	$\begin{pmatrix} -1.382 & -0.541 & 0.541 \\ -0.541 & -1.382 & 0.541 \\ 0.541 & 0.541 & -1.382 \end{pmatrix}$	

symmetry analysis or through molecular dynamics, as the latter cannot deliver a detailed characterization for temperatures well below melting mainly because some of the transformations require dwelling metastable states that cannot endure in these high temperatures and can only play a dynamical and structural role at a lower temperature.

Accelerated methods such as the kinetic ART provides detailed and rich information regarding mechanisms that we did not know existed until now. The systematic use of such methods will continue to enrich significantly our understanding of diffusion at the atomistic level in materials.

The most recent packages for k-ART and ARTn are available freely upon request [80].

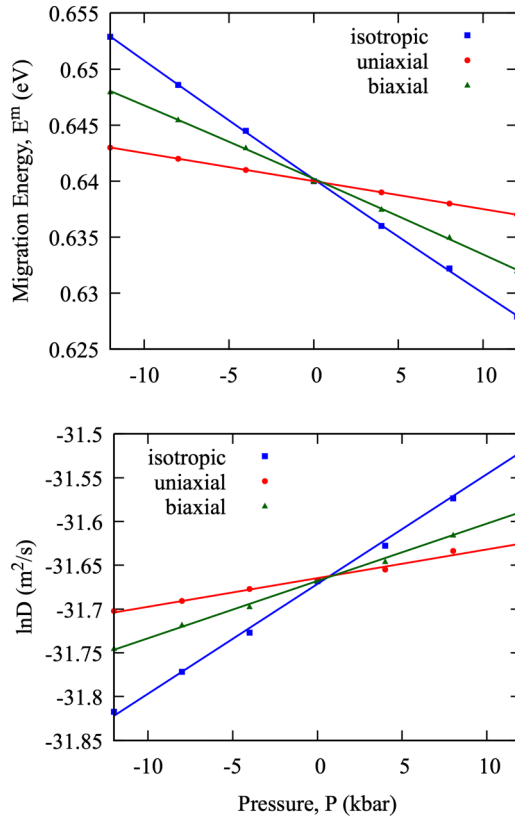


FIG. 14. Variation migration energy E^m (top) and diffusion coefficient D (bottom) as a function of pressure for monovacancy in α -iron at temperature 600 K: Under isotropic pressure (blue square), pressure along the x direction (red circle) and pressure along the y and z directions (green triangle).

ACKNOWLEDGMENTS

We would like to thank the anonymous referee for their very valuable suggestions with respect to the elastic dipole analysis. This work has been supported by the Qatar National Research Fund (QNRF) through the National Priorities Research Program under Project No. NPRP10-0105-170118 and the Canada Research Chairs program and by a discovery grant (NM) from the Natural Sciences and Engineering Research Council of Canada (NSERC). We are grateful to Digital Research Alliance of Canada for generous allocations of computer resources.

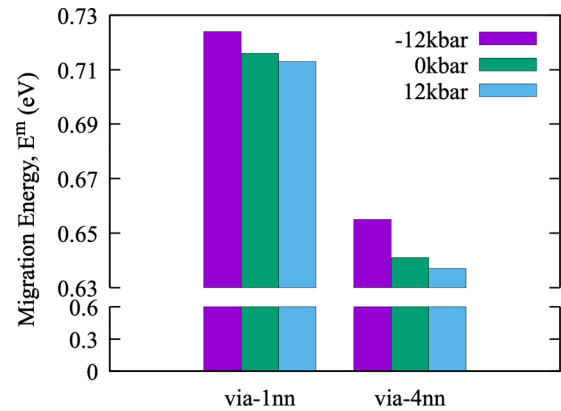


FIG. 15. Variation in migration energy E^m of two most dominant diffusion mechanisms [transition to 2NN (GS) to 1NN to 2NN (new GS) and 2NN (GS) to 4NN to 2NN (new GS)] as a function of isotropic pressure for divacancy in α -iron.

- [1] W. Sun, Y. Zhu, R. Marceau, L. Wang, Q. Zhang, X. Gao, and C. Hutchinson, Precipitation strengthening of aluminum alloys by room-temperature cyclic plasticity, *Science* **363**, 972 (2019).
- [2] M. Nagumo and K. Takai, The predominant role of strain-induced vacancies in hydrogen embrittlement of steels: Overview, *Acta Mater.* **165**, 722 (2019).
- [3] J. Heikinheimo, K. Mizohata, J. Räisänen, T. Ahlgren, P. Jalkanen, A. Lahtinen, N. Catarino, E. Alves, and F. Tuomisto, Direct observation of mono-vacancy and self-interstitial recovery in tungsten, *APL Mater.* **7**, 021103 (2019).
- [4] A. Bhattacharya, E. Meslin, J. Henry, A. Barbu, S. Poissonnet, and B. Décamps, Effect of chromium on void swelling in ion irradiated high purity Fe–Cr alloys, *Acta Mater.* **108**, 241 (2016).
- [5] F. Ferroni, X. Yi, K. Arakawa, S. P. Fitzgerald, P. D. Edmondson, and S. G. Roberts, High temperature annealing of ion irradiated tungsten, *Acta Mater.* **90**, 380 (2015).
- [6] J. Park, H. Huang, R. Siegel, and R. Balluffi, A quantitative study of vacancy defects in quenched tungsten by combined field-ion microscopy and electrical resistometry, *Philos. Mag. A* **48**, 397 (1983).
- [7] K. Rasch, R. Siegel, and H. Schultz, Quenching and recovery investigations of vacancies in tungsten, *Philos. Mag. A* **41**, 91 (1980).
- [8] C. Sun, A short review of defect superlattice formation in metals and alloys under irradiation, *J. Nucl. Mater.* **559**, 153479 (2021).
- [9] J. Evans, Observations of a regular void array in high purity molybdenum irradiated with 2 MeV nitrogen ions, *Nature (London)* **229**, 403 (1971).
- [10] C. Sun, C. Jiang, E. Jossou, M. Topsakal, S. K. Gill, L. E. Ecker, and J. Gan, Self-assembly of solid nanoclusters in molybdenum under gas ion implantation, *Scr. Mater.* **194**, 113651 (2021).
- [11] C. Sun, D. J. Sprouster, Y. Zhang, D. Chen, Y. Wang, L. E. Ecker, and J. Gan, Formation window of gas bubble superlattice in molybdenum under ion implantation, *Phys. Rev. Mater.* **3**, 103607 (2019).
- [12] L. Chen, W. Liu, L. Yu, Y. Cheng, K. Ren, H. Sui, X. Yi, and H. Duan, Probabilistic and constitutive models for ductile-to-brittle transition in steels: A competition between cleavage and ductile fracture, *J. Mech. Phys. Solids* **135**, 103809 (2020).
- [13] A. H. Hameed, S. Rohani, W. Yu, C. Tai, and C. Lan, Surface defects and mechanical hardness of rapidly grown dast crystals, *J. Cryst. Growth* **297**, 146 (2006).
- [14] Y. Cui, G. Po, and N. Ghoniem, Does irradiation enhance or inhibit strain bursts at the submicron scale? *Acta Mater.* **132**, 285 (2017).
- [15] X. Wu, X. Pan, M. Li, and J. F. Stubbins, Modeling tensile response and flow localization effects in 316SS after exposure to spallation and fission irradiation environments, *J. Nucl. Mater.* **343**, 302 (2005).
- [16] W. Kohn and L. J. Sham, Self-consistent equations including exchange and correlation effects, *Phys. Rev.* **140**, A1133 (1965).
- [17] F. Djurabekova, L. Malerba, R. C. Pasianot, P. Olsson, and K. Nordlund, Kinetics versus thermodynamics in materials modeling: The case of the di-vacancy in iron, *Philos. Mag.* **90**, 2585 (2010).
- [18] D. Kandaskalov, C. Mijoule, and D. Connétable, Study of multivacancies in alpha Fe, *J. Nucl. Mater.* **441**, 168 (2013).
- [19] C.-C. Fu, J. D. Torre, F. Willaime, J.-L. Bocquet, and A. Barbu, Multiscale modelling of defect kinetics in irradiated iron, *Nat. Mater.* **4**, 68 (2005).
- [20] P. M. Derlet, D. Nguyen-Manh, and S. L. Dudarev, Multiscale modeling of crowdion and vacancy defects in body-centered-cubic transition metals, *Phys. Rev. B* **76**, 054107 (2007).
- [21] L. Wan, X. Ye, X. Cao, S. Jin, and T. Gao, First-principles study of helium in austenitic Fe 6.3 at% Cr alloys: Structural, stability, energetics, and clustering with vacancies, *Mater. Today Commun.* **29**, 102837 (2021).
- [22] L. Ventelon, F. Willaime, C.-C. Fu, M. Heran, and I. Ginoux, *Ab initio* investigation of radiation defects in tungsten: Structure of self-interstitials and specificity of di-vacancies compared to other bcc transition metals, *J. Nucl. Mater.* **425**, 16 (2012).
- [23] J. Hou, X.-S. Kong, X. Wu, J. Song, and C. Liu, Predictive model of hydrogen trapping and bubbling in nanovoids in bcc metals, *Nat. Mater.* **18**, 833 (2019).
- [24] B. J. Alder and T. E. Wainwright, Studies in molecular dynamics. I. general method, *J. Chem. Phys.* **31**, 459 (1959).
- [25] A. F. Voter, Classically exact overlayer dynamics: Diffusion of rhodium clusters on rh (100), *Phys. Rev. B* **34**, 6819 (1986).
- [26] A. F. Voter, Introduction to the kinetic monte carlo method, in *Radiation Effects in Solids* (Springer, Berlin, 2007), pp. 1–23.
- [27] F. El-Mellouhi, N. Mousseau, and L. J. Lewis, Kinetic activation-relaxation technique: An off-lattice self-learning kinetic Monte Carlo algorithm, *Phys. Rev. B* **78**, 153202 (2008).
- [28] N. Mousseau, L. K. Béland, P. Brommer, F. El-Mellouhi, J. F. Joly, G. K. N'tsouaglo, O. A. Restrepo, and M. Trochet, Following atomistic kinetics on experimental timescales with the kinetic Activation Relaxation Technique, *Comput. Mater. Sci.* **100**, 111 (2015).
- [29] J.-F. Joly, L. K. Béland, P. Brommer, F. El-Mellouhi, and N. Mousseau, Optimization of the kinetic activation-relaxation technique, an off-lattice and self-learning kinetic Monte-Carlo method, in *Journal of Physics: Conference Series*, Vol. 341 (IOP Publishing, Bristol, 2012), p. 012007.
- [30] M. M. Rahman, F. El-Mellouhi, O. Bouhali, C. S. Becquart, and N. Mousseau, Pressure effect on diffusion of carbon at the 85.91°(100) symmetric tilt grain boundary of α -iron, *Phys. Rev. Mater.* **5**, 043605 (2021).
- [31] S. Mahmoud and N. Mousseau, Long-time point defect diffusion in ordered nickel-based binary alloys: How small kinetic differences can lead to completely long-time structural evolution, *Materialia* **4**, 575 (2018).
- [32] O. A. Restrepo, N. Mousseau, M. Trochet, F. El-Mellouhi, O. Bouhali, and C. S. Becquart, Carbon diffusion paths and segregation at high-angle tilt grain boundaries in α -Fe studied by using a kinetic activation-relation technique, *Phys. Rev. B* **97**, 054309 (2018).
- [33] F. Djurabekova, L. Malerba, C. Domain, and C. Becquart, Stability and mobility of small vacancy and copper-vacancy clusters in bcc-Fe: An atomistic kinetic Monte Carlo study, *Nucl. Instrum. Methods Phys. Res., Sect. B* **255**, 47 (2007).
- [34] J. Hou, Y.-W. You, X.-S. Kong, J. Song, and C. Liu, Accurate prediction of vacancy cluster structures and energetics in bcc transition metals, *Acta Mater.* **211**, 116860 (2021).
- [35] L. Malerba, N. Anento, J. P. Balbuena, C. Becquart, N. Castin, M. J. Caturla, C. Domain, C. Guerrero, C. Ortiz, B. Pannier *et al.*, Physical mechanisms and parameters for models of

- microstructure evolution under irradiation in Fe alloys—Part I: Pure Fe, *Nucl. Mater. Energy* **29**, 101069 (2021).
- [36] M. Gilbert, Z. Yao, M. Kirk, M. Jenkins, and S. Dudarev, Vacancy defects in Fe: Comparison between simulation and experiment, *J. Nucl. Mater.* **386-388**, 36 (2009).
- [37] A. E. Sand, J. Byggmästar, A. Zitting, and K. Nordlund, Defect structures and statistics in overlapping cascade damage in fusion-relevant bcc metals, *J. Nucl. Mater.* **511**, 64 (2018).
- [38] D. Kulikov, L. Malerba, and M. Hou, On the binding energies and configurations of vacancy and copper–vacancy clusters in bcc Fe–Cu: A computational study, *Philos. Mag.* **86**, 141 (2006).
- [39] N. Castin, M. Pascuet, and L. Malerba, Mobility and stability of large vacancy and vacancy–copper clusters in iron: An atomistic kinetic Monte Carlo study, *J. Nucl. Mater.* **429**, 315 (2012).
- [40] C. Domain, C. Becquart, and L. Malerba, Simulation of radiation damage in Fe alloys: An object kinetic Monte Carlo approach, *J. Nucl. Mater.* **335**, 121 (2004).
- [41] P. Brommer, L. K. Béland, J.-F. Joly, and N. Mousseau, Understanding long-time vacancy aggregation in iron: A kinetic activation-relaxation technique study, *Phys. Rev. B* **90**, 134109 (2014).
- [42] L. Malerba, M.-C. Marinica, N. Anento, C. Björkas, H. Nguyen, C. Domain, F. Djurabekova, P. Olsson, K. Nordlund, A. Serra *et al.*, Comparison of empirical interatomic potentials for iron applied to radiation damage studies, *J. Nucl. Mater.* **406**, 19 (2010).
- [43] F. Wan, S. Ohnuki, H. Takahashi, T. Takeyama, and R. Nagasaki, Vacancy loop formation in hydrogen-ion-implanted alpha-iron, *Philosophical Magazine A* **53**, L21 (1986).
- [44] M. Gilbert, S. Dudarev, P. Derlet, and D. Pettifor, Structure and metastability of mesoscopic vacancy and interstitial loop defects in iron and tungsten, *J. Phys.: Condens. Matter* **20**, 345214 (2008).
- [45] N. Soneda, S. Ishino, and T. D. De la Rubia, Vacancy loop formation by ‘cascade collapse’ in α -Fe: A molecular dynamics study of 50 keV cascades, *Philos. Mag. Lett.* **81**, 649 (2001).
- [46] J. R. Beeler, Jr. and R. Johnson, Vacancy clusters in α -iron, *Phys. Rev.* **156**, 677 (1967).
- [47] L. K. Béland, P. Brommer, F. El-Mellouhi, J.-F. Joly, and N. Mousseau, Kinetic activation-relaxation technique, *Phys. Rev. E* **84**, 046704 (2011).
- [48] B. D. McKay and A. Piperno, Practical graph isomorphism, II, *J. Symbol. Comput.* **60**, 94 (2014).
- [49] G. T. Barkema and N. Mousseau, Event-Based Relaxation of Continuous Disordered Systems, *Phys. Rev. Lett.* **77**, 4358 (1996).
- [50] R. Malek and N. Mousseau, Dynamics of Lennard-Jones clusters: A characterization of the activation-relaxation technique, *Phys. Rev. E* **62**, 7723 (2000).
- [51] E. Machado-Charry, L. K. Béland, D. Caliste, L. Genovese, T. Deutsch, N. Mousseau, and P. Pochet, Optimized energy landscape exploration using the *ab initio* based activation-relaxation technique, *J. Chem. Phys.* **135**, 034102 (2011).
- [52] H. Eyring, The activated complex and the absolute rate of chemical reactions, *Chem. Rev.* **17**, 65 (1935).
- [53] M. G. Evans and M. Polanyi, Some applications of the transition state method to the calculation of reaction velocities, especially in solution, *Trans. Faraday Soc.* **31**, 875 (1935).
- [54] K. J. Laidler and M. C. King, Development of transition-state theory, *J. Phys. Chem.* **87**, 2657 (1983).
- [55] B. Puchala, M. L. Falk, and K. Garikipati, An energy basin finding algorithm for kinetic Monte Carlo acceleration, *J. Chem. Phys.* **132**, 134104 (2010).
- [56] S. Plimpton, Fast parallel algorithms for short-range molecular dynamics, *J. Comput. Phys.* **117**, 1 (1995).
- [57] LAMMPS, <http://lammmps.sandia.gov>.
- [58] M. Mendeleev, S. Han, D. Srolovitz, G. Ackland, D. Sun, and M. Asta, Development of new interatomic potentials appropriate for crystalline and liquid iron, *Philos. Mag.* **83**, 3977 (2003).
- [59] E. Clouet, C. Varvenne, and T. Jourdan, Elastic modeling of point-defects and their interaction, *Comput. Mater. Sci.* **147**, 49 (2018).
- [60] R. G. Veiga, M. Perez, C. Becquart, E. Clouet, and C. Domain, Comparison of atomistic and elasticity approaches for carbon diffusion near line defects in α -iron, *Acta Mater.* **59**, 6963 (2011).
- [61] P.-W. Ma and S. L. Dudarev, Effect of stress on vacancy formation and migration in body-centered-cubic metals, *Phys. Rev. Mater.* **3**, 063601 (2019).
- [62] C. Kittel, *Introduction to Solid State Physics* (Wiley, Hoboken, NJ, 2005).
- [63] H. Schaefer, Investigation of thermal equilibrium vacancies in metals by positron annihilation, *Phys. Status Solidi. A* **102**, 47 (1987).
- [64] C. Domain and C. S. Becquart, *Ab initio* calculations of defects in Fe and dilute Fe-Cu alloys, *Phys. Rev. B* **65**, 024103 (2001).
- [65] P. Olsson, C. Domain, and J. Wallenius, *Ab initio* study of Cr interactions with point defects in bcc Fe, *Phys. Rev. B* **75**, 014110 (2007).
- [66] See Supplemental Material at <http://link.aps.org/supplemental/10.1103/PhysRevMaterials.7.093602> for additional figures and tables.
- [67] K. Sugita, M. Mizuno, H. Araki, Y. Shirai, T. Omura, K. Tomatsu, and Y. Sakiyama, Review of positron lifetime studies of lattice defects formed during tensile deformation in a hydrogen environment, *ISIJ International* **61**, 1056 (2021).
- [68] M. Puska and R. Nieminen, Defect spectroscopy with positrons: A general calculational method, *J. Phys. F: Met. Phys.* **13**, 333 (1983).
- [69] H. Ohkubo, Z. Tang, Y. Nagai, M. Hasegawa, T. Tawara, and M. Kiritani, Positron annihilation study of vacancy-type defects in high-speed deformed Ni, Cu and Fe, *Mater. Sci. Eng. A* **350**, 95 (2003).
- [70] C. Lu, L. Niu, N. Chen, K. Jin, T. Yang, P. Xiu, Y. Zhang, F. Gao, H. Bei, S. Shi *et al.*, Enhancing radiation tolerance by controlling defect mobility and migration pathways in multicomponent single-phase alloys, *Nat. Commun.* **7**, 13564 (2016).
- [71] T. Diaz de la Rubia, H. M. Zbib, T. A. Khraishi, B. D. Wirth, M. Victoria, and M. J. Caturla, Multiscale modelling of plastic flow localization in irradiated materials, *Nature (London)* **406**, 871 (2000).
- [72] R. S. Averback and T. D. De La Rubia, Displacement damage in irradiated metals and semiconductors, *Solid State Phys. Adv. Res. Appl.* **51**, 281 (1997).

- [73] R. Gul, U. Roy, S. Egarievwe, A. Bolotnikov, G. Camarda, Y. Cui, A. Hossain, G. Yang, and R. James, Point defects: Their influence on electron trapping, resistivity, and electron mobility-lifetime product in $\text{CdTe}_x\text{Se}_{1-x}$ detectors, *J. Appl. Phys.* **119**, 025702 (2016).
- [74] P. Klemens, Thermal resistance due to point defects at high temperatures, *Phys. Rev.* **119**, 507 (1960).
- [75] A. Chakrabarty, O. Bouhali, N. Mousseau, C. S. Becquart, and F. El-Mellouhi, Insights on finite size effects in *ab initio* study of Co adsorption and dissociation on Fe 110 surface, *J. Appl. Phys.* **120**, 055301 (2016).
- [76] P. W. Ma and S. L. Dudarev, Universality of point defect structure in body-centered cubic metals, *Phys. Rev. Mater.* **3**, 013605 (2019).
- [77] J. S. Wróbel, M. R. Zemła, D. Nguyen-Manh, P. Olsson, L. Messina, C. Domain, T. Wejznanowski, and S. L. Dudarev, Elastic dipole tensors and relaxation volumes of point defects in concentrated random magnetic Fe-Cr alloys, *Comput. Mater. Sci.* **194**, 110435 (2021).
- [78] A. Sivak, V. Romanov, and V. Chernov, Diffusion of self-point defects in body-centered cubic iron crystal containing dislocations, *Crystallogr. Rep.* **55**, 97 (2010).
- [79] R. Meyer, G. dos Santos, R. Aparicio, E. M. Bringa, and H. M. Urbassek, Influence of vacancies on the temperature-dependent magnetism of bulk Fe: A spin-lattice dynamics approach, *Comput. Condens. Matter* **31**, e00662 (2022).
- [80] Please contact N. Mousseau (normand.mousseau@umontreal.ca).